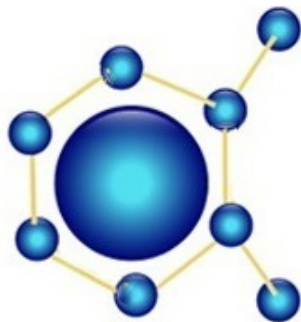




SETCOR
Conferences & Events



2nd Edition

S M S
Smart Materials and Surfaces
KOREA 2016
Conference

23 - 25 March, 2016 | Songdo Convensia, Incheon, Korea

SMS Korea 2016 International Conference Proceeding

<http://www.setcor.org/conferences/SMS-KOREA-2016>

ZnO-based UV detector performance improvement

Khakhulin D.A.¹, Ageev O.A.¹, Zamburg E.G.¹, Varzarev Yu.N.¹, Jong-Gul Yoon²

¹ Southern federal university, Institute of Nanotechnology, Electronics and Electronics Equipment Instrumentation, Taganrog, Shevchenko st., 2

² University of Suwon, San 2-2, Wau-ri, Bongdam-eup, Hwasung-si, Gyeonggi-do 445-743, Korea

Abstract:

Sensors of UV radiation are important elements of many systems in the defense and aerospace industries. Thus, it is a remarkable goal to improve the basic parameters of these devices. ZnO is one of the possible alternatives for currently used materials in UV detection applications. This transparent material has the optical band gap of 3.37 eV, which enables to detect radiation with a wavelength of about 375 nm (Zamburg *et al.*; 2012). We report the investigation of an influence of deposition process' parameters, upon the UV detection performance of nanocrystalline ZnO films. Films were produced by aerosol assisted chemical vapor deposition. (Yoon *et al.*; 1998) By varying the temperature and the type of substrate we controlled crystallographic structure of ZnO film, and, as a result, photosensitivity. Eight samples were produced. Four samples were grown on amorphous ITO under temperatures 300°C, 350°C, 400°C and 450°C. Investigation of the parameters of these samples showed, that it is necessary to use two temperatures: 300°C and 420°C. We produced four more samples: on sapphire under 300°C, on sapphire under 420°C, on sapphire under 300°C with introduction of Pt and on Si under 300°C with introduction of Pt. These are sample 5, 6, 7 and 8, respectively. Structural and electrical properties of the films were studied. Figure 1 shows current-on-time characteristics of samples 5-8. We report production of the detector with a high photoresponse and discuss how substrate, Pt nanoparticles and deposition temperature influence photosensitivity of ZnO films obtained by AACVD process. Also, results are compared with some other published studies (Transley, Neeley; 1984).

Key words: ZnO, thin film, UV detector, AACVD

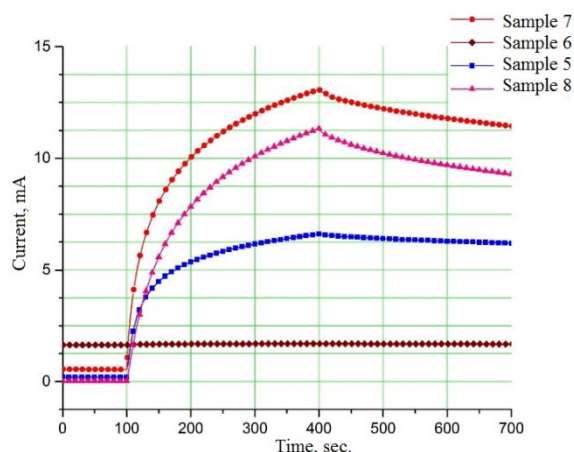


Figure 1 Current-on-time characteristics of samples 5-8. It shows slow growth and decline of photocurrent in samples 5, 7 and 8 and almost no response in sample 6

References:

Ageev O.A., Dostanko A.P., Golosov D.A., Zavadski S.M., Zamburg E.G., Vakulov D.E., and Vakulov Z.E. (2014), Electrical and optical properties of zinc-oxide films deposited by the ion-beam sputtering of an oxide target, *Semiconductors*, vol. 48, №9, P. 1242–1247.

Jong-Gul Yoon, Hun Kyoo Oh, Young Jik Kwag (1998), Structural and optical properties of TiO₂-SiO₂ composite films prepared by aerosol-assisted chemical-vapor deposition, *Journal of the Korean Physical Society*, vol. 33, №6, P. 699-704.

Tansley T.L., Neely D.F. (1984), Adsorption, desorption and conductivity of sputtered zinc oxide thin films, *Thin Solid Films* №121, P. 95-107.

Stable Colloidal Nanographene for Biomedical Applications

Xingyu He¹, Vesselin Shanov^{1,2} and Yoonjee Park^{1,a}

¹Department of Biomedical, Chemical and Environmental Engineering, University of Cincinnati, 2600 Clifton Ave., Cincinnati, OH 45221

²Department of Mechanical and Materials Engineering, University of Cincinnati, 2600 Clifton Ave., Cincinnati, OH 45221

Abstract. Nano-sized graphene has attracted great interests in various fields including medicine because of its unique intrinsic physical properties and small size. However, dispersibility of nanographene in aqueous media is poor and this creates a challenge in utilizing nanographene in biomedical applications. This paper demonstrates that stable nanographene aqueous dispersions were obtained by incorporating graphene into liposome layers. UV and Raman measurements proved the existence of multi-layered graphene in the obtained nanostructure. The diameter of liposomal graphene was around 100 nm and the created colloidal suspension was stable for days. Nano-sized graphene was used as a shell material of nanodroplets, thus demonstrating the potential of utilizing the created aqueous dispersible nanostructure for biomedical applications.

1. Introduction

Graphene has attracted great interests in various fields including biomedical applications due to its high surface area (2630 m²/g) and delocalized electrons with a high capacity for loading of aromatic drugs via p-p stacking [1]. In addition, graphene has high near-infrared absorbance properties, thus it can be potentially utilized for photothermal therapy. However, for biomedical applications, graphene has to be hydrophilic, well dispersed in the body, and the particle size has to be in the “nano” range. It is challenging to produce nanographene dispersed in aqueous media without aggregation because this material in pristine form is very hydrophobic. Most studies on graphene in the biomedical field have used surface-modified/functionalized graphene, such as graphene oxide (GO) [2, 3]. Surface-modified graphene involves breakdown of the continuous honeycomb backbone of pristine (non-functionalized) graphene compromising several of the typical properties of the original materials. In fact, numerous reports have demonstrated that pristine graphene exhibits higher conductivity than chemically converted graphene due to fewer defects. Therefore, it would be beneficial to produce nano-sized pristine graphene dispersed in aqueous media in order to utilize this material in the biomedical fields.

In this study, we successfully pursued to create colloidal nanographene using liposomes. As described

below, nano-sized graphene incorporated in liposome bilayers is stably dispersed in an aqueous medium. The characteristics of the liposomal graphene were measured by various analytical instruments. Finally, the colloidal nanographene was utilized as a shell material of nanodroplets designed for drug delivery vehicle.

2. Methods

2.1 Materials

Dipalmitoylphosphatidylcholine (DPPC) and PEG-5000 modified distearoylphosphatidylethanolamine (DSPE-PEG-5000) were purchased from Avanti Polar Lipids, Inc. (Alabaster, AL). Graphite powder (<20 μ m, synthetic) was purchased from Sigma Aldrich.

2.2. Liposomal nanographene synthesis

The liposomal-graphene synthesis involves three steps: 1. Liposome synthesis, 2. Graphene suspension, and 3. Combination of liposome and graphene suspension to create liposomal graphene. To synthesize a liposome dispersion, a dry film of DPPC and DSPE-PEG-5000 (85:15 mol%) was sonicated with DI water for 10 min by a micro-probe. For the graphene aqueous suspension, 3 mg (\pm 0.2) of graphite powder in DI water

^aCorresponding author: parkye@ucmail.uc.edu

was sonicated for 90 min by the micro-probe in an ice-bath to prevent evaporation due to boiling. Lastly, a mixture of the liposome dispersion and the graphene suspension (1:1 v/v) was sonicated for 90 min in an ice-bath. The resulting suspension was centrifuged at 5000 rpm for 15 min to remove non-liposome coated graphene.

2.2. Characterization of liposomal nanographene

2.2.1. UV-vis spectroscopy measurement

Samples were placed in a UV-transparent 96 well plate (Corning™ 96-Well UV-Transparent Half-Area Microplates) for UV-vis spectroscopy measurement using SpectraMax M2e (Sunnyvale, CA).

2.2.2. Raman spectroscopy measurement

A sample was prepared on a copper plate by air-dry and measured by a 514 nm He-Ne laser with a laser spot size of 1 mm^2 (Renishaw inVia Raman Microscope, Hoffman Estates, IL).

2.2.3. Atomic Force Microscopy (AFM) measurement

Samples were prepared on a cleaned silicon wafer by air-dry. AFM analysis was performed using Veeco Dimension 3100 in tapping mode at room temperature, using a n-type silicon cantilevers (NSC16/50). The scan rate was 0.996 Hz, and the whole scan area was $5 \times 5 \text{ }\mu\text{m}^2$.

2.2.4. Dynamic Light Scattering (DLS) measurement and stability test

Hydrodynamic diameters of samples were measured by NanoBrook Omni (Brookhaven Instruments Corporation, Holtsville, NY) three times for each sample at room temperature and each measurement took 1 min.

2.3. Nanodroplet synthesis

Liposomal nanographene was mixed with perfluorocarbon (PFC) and sonicated by the micro-probe in an ice-bath for 3 min (10 sec on, 20 sec off mode) to create nanographene-coated nanodroplets. Then the product was centrifuged at 2000 rpm for 5 min. The supernatant was replaced with the same volume of DI water and resuspended. The centrifugation and

purification process was repeated three times to ensure removal of liposomal nanographene in the suspension.

3. Results

3.1. Liposomal nanographene

Colloidal nanographene was successfully synthesized using liposomes. Nanographene incorporated into liposome layers was detected by UV-vis and Raman spectroscopy (**Figure 1**). UV-vis spectrum of the liposomal graphene showed peaks from both the liposome dispersion and the graphene suspension. The liposome dispersion (Sample 1) showed a typical peak of liposome at 230 nm, as reported in a reference [4]. The graphene suspension from Sample 2 revealed a peak at 270 nm. The liposomal graphene has peaks at 225 nm and 260 nm, which are characteristics of liposome and graphene, respectively.

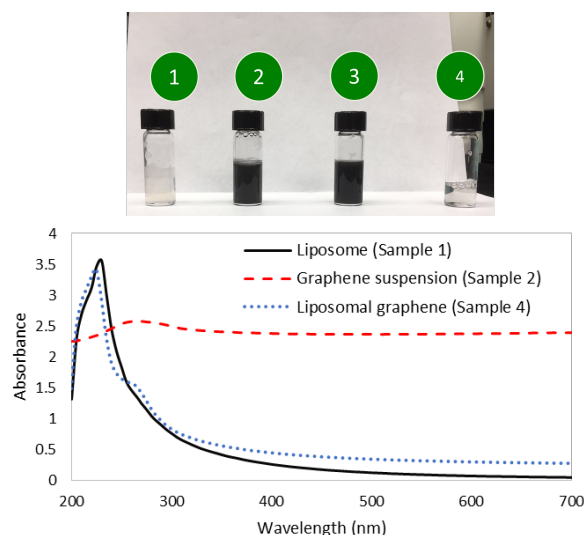


Figure 1. Optical images of the samples and related UV-vis spectra: Sample 1: Liposome dispersion; Sample 2: Graphene suspension; Sample 3: Liposomal graphene before centrifugation; Sample 4: Liposomal graphene after centrifugation, supernatant of Sample 3.

Raman spectrum of liposomal graphene showed a G peak greater than a 2D peak, indicating that nanographene in the liposome layer is multi-layered (**Figure 2**). In addition, a D peak in the spectrum implies small amount of sp³ bonded carbon in the nanographene is present.

The size of liposomal graphene measured by DLS was 116 nm (standard deviation $\sigma=0.18$). The stability against aggregation was examined by DLS (**Figure 3**).

^aCorresponding author: parkye@ucmail.uc.edu

The size did not change for 7 days, indicating the liposomal graphene is stable at least for days.

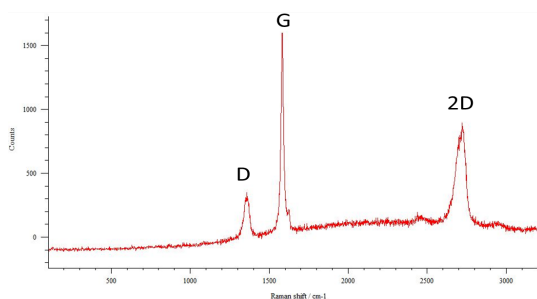


Figure 2. Raman spectrum of liposomal graphene (Sample 3).

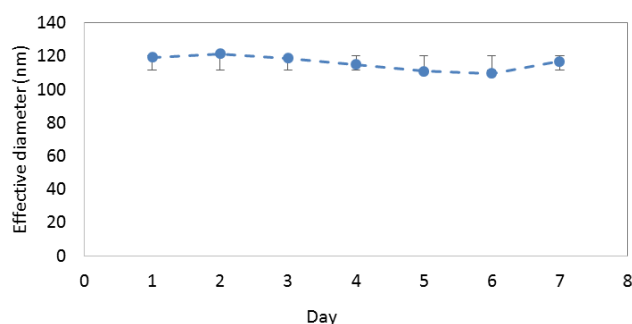


Figure 3. DLS results demonstrating stability of the liposomal graphene suspension (Sample 4).

AFM image and the cross-section analysis showed the liposomal graphene size ranged 40 to 140 nm in diameter and the height when dried ranged from 4 to 10 nm (**Figure 4**).

Lastly, the liposomal graphene was utilized to create nanodroplets as a shell material. The UV spectrum of the nanodroplets showed a peak at 265 nm, indicating incorporation of nanographene.

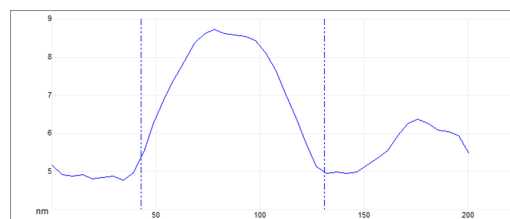
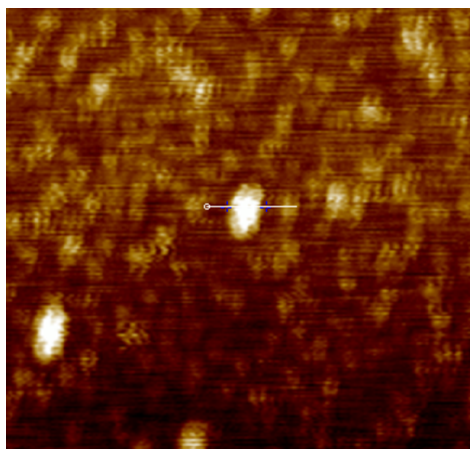


Figure 4. AFM images ($1.43 \times 1.43 \mu\text{m}^2$) and cross-section along the cross line in the image (white line).

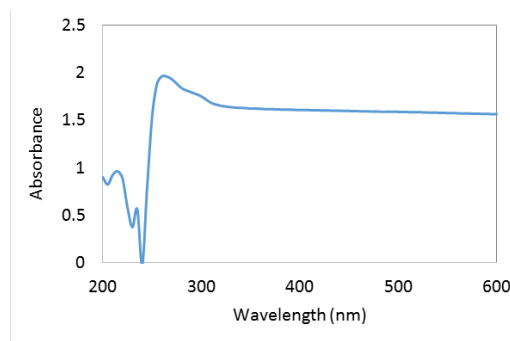


Figure 5. UV spectrum for nanographene-coated nanodroplets.

4. Discussion

The UV spectrum of the liposomal nanographene has a peak at 260 nm, which is different from the peak of graphene oxide at 230 nm [5, 6]. These results indicate that the nanographene consists of pristine graphene sheets instead of oxidized graphene. Note that the peak at 230 nm for the liposomes shifted to 225 nm for the liposomal graphene. The blue shift is probably due to insertion of hydrophobic nanographene in hydrocarbon chains of the liposomes. Zhao and Kinnunen also observed blue shift of a liposome peak in the UV region by hydrophobic peptide insertion [7]. We speculate this blue shift is due to changes in hydrophobic interaction of lipid layer structure. A similar shift was observed for graphene. The peak for graphene shifted to shorter wavelength from 270 nm to 260 nm when the nanographene was placed in liposome layers, probably also due to changes in hydrophobic interactions of nanographene sheets by the incorporation with lipid layers. The Raman spectrum showed a D peak corresponding sp^3 bonds, which may be mainly located at the edges of the nanographene. The intensity of the 2D peak is less than the intensity of the G peak, indicating the graphene sheets are multi-layered [8].

The colloidal nanographene dispersion in an aqueous medium was stabilized by liposomes. The liposome used in the study consists of 15 mol% of polymeric lipids, which provides steric repulsion between liposomes. The size of the liposomal graphene

was bigger than the liposome (Sample 1) approximately by 10 nm. Graphene incorporation into liposome layer seemed to affect the size of the liposomes.

The size of nanographene incorporated in liposome layers should be smaller than the liposome size which ranges from 40 nm to 140 nm based on AFM results. The exact size of nanographene will be evaluated using transmission electron microscope (TEM) in a future study. The size of liposomal graphene measured by AFM was comparable to the one measured by DLS. DLS technique uses hydrodynamic diameter, which results in greater values than the size measured by optical techniques [9].

Lastly, nanodroplet synthesis utilizing the liposomal graphene demonstrated that the nanographene can be easily implemented in various forms and structures and stably dispersed in aqueous media. This results shows potential of utilizing liposomal graphene to create nanographene-containing structures especially useful for biomedical applications.

5. Conclusions

Colloidal nanographene dispersed in aqueous media has been successfully produced using liposomes. The liposomal nanographene was stable for days in DI water. The liposomal nanographene was easily transformed to produce nanographene-coated nanodroplets, indicating potential of utilizing liposomal nanographene for biomedical applications.

Acknowledgements

References

- [1] K. Yang, L. Feng, Z. Liu, The advancing uses of nano-graphene in drug delivery, *Expert Opinion on Drug Delivery*, 12 (2015) 601-612.
- [2] Y. Wang, K. Wang, J. Zhao, X. Liu, J. Bu, X. Yan, R. Huang, Multifunctional Mesoporous Silica-Coated Graphene Nanosheet Used for Chemo-Photothermal Synergistic Targeted Therapy of Glioma, *Journal of the American Chemical Society*, 135 (2013) 4799-4804.
- [3] L. Feng, X. Yang, X. Shi, X. Tan, R. Peng, J. Wang, Z. Liu, Polyethylene Glycol and Polyethylenimine Dual-Functionalized Nano-Graphene Oxide for Photothermally Enhanced Gene Delivery, *Small*, 9 (2013) 1989-1997.
- [4] R.A.R. Samaa M. Elfaramawy, Spectrophotometric Studies on Antioxidants-Doped Liposomes, *Journal of American Science* 7(2011) 363-369.
- [5] P. Huang, C. Xu, J. Lin, C. Wang, X.S. Wang, C.L. Zhang, X.J. Zhou, S.W. Guo, D.X. Cui, Folic Acid-

conjugated Graphene Oxide loaded with Photosensitizers for Targeting Photodynamic Therapy, *Theranostics*, 1 (2011) 240-250.

[6] J. Li, C.-y. Liu, Y. Liu, Au/graphene hydrogel: synthesis, characterization and its use for catalytic reduction of 4-nitrophenol, *Journal of Materials Chemistry*, 22 (2012) 8426-8430.

[7] H. Zhao, P.K.J. Kinnunen, Binding of the Antimicrobial Peptide Temporin L to Liposomes Assessed by Trp Fluorescence, *Journal of Biological Chemistry*, 277 (2002) 25170-25177.

[8] A. Das, B. Chakraborty, A.K. Sood, Raman spectroscopy of graphene on different substrates and influence of defects, *Bulletin of Materials Science*, 31 (2008) 579-584.

[9] Y.C. Park, J.B. Smith, T. Pham, R.D. Whitaker, C.A. Sucato, J.A. Hamilton, E. Bartolak-Suki, J.Y. Wong, Effect of PEG molecular weight on stability, T2 contrast, cytotoxicity, and cellular uptake of superparamagnetic iron oxide nanoparticles (SPIONs), *Colloids and Surfaces B: Biointerfaces*, 119 (2014) 106-114.

To obtain the La (Fe, Si)₁₃ phase in as-casting La-Fe-Si magnetocaloric alloys

Liang Yang¹, Yujin Huang¹, Zhenni Zhou¹, Jun Li^{1,2*}, Jianguo Li¹

¹School of Materials Science and Engineering, Shanghai Jiao Tong University, Shanghai 200240, China

²Collaborative Innovation Center for Advanced Ship and deep-Sea Exploration, Shanghai Jiao Tong University, Shanghai 200240, China

*Corresponding authors, E-mail: li.jun@sjtu.edu.cn (J.Li). Tel.& fax: 0086-21-54744119. +86-15601897272

Abstract

The La-Fe-Si magnetocaloric alloys are considered as a promising room temperature magnetic refrigerant. It is shown that their giant magnetocaloric effect originates from the NaZn₁₃-type La (Fe, Si)₁₃ phase. However, it is a challenge to obtain the La (Fe, Si)₁₃ phase through a conventional solidification. To obtain the La (Fe, Si)₁₃ single phase, one usually spends seven days on homogenizing the as-solidified La-Fe-Si alloys that is constituted of the α -Fe and LaFeSi phases. In this case, the annealing time is too long to meet the requirements of practical applications. Many efforts have been put to explore some advanced solidification processes for increasing the volume fraction of La (Fe, Si)₁₃ phase, such as melt-spun, drop-tube processing and melt-extract wires, but there is no investigation for bulk castings. In this work, we greatly increase the volume fraction of the La (Fe, Si)₁₃ phase in the La-Fe-Si bulk casting by a zone melting liquid metal cooling (ZMLMC) directional solidification, which is supposed to shorten the annealing time. The microstructure observation reveals that the volume fraction of the La (Fe, Si)₁₃ phase is about 30.5% and the remnant is the α -Fe phase. This is higher than the volume fraction (20%) of the La (Fe, Si)₁₃ phase in the La-Fe-Si magnetocaloric alloys prepared by the drop-tube processing. Interestingly, a composition segregation is distinctly observed in the La (Fe, Si)₁₃ phase, of which the Si content is about 20.3% much higher than the predicted value.

Keywords: La-Fe-Si alloys, directional solidification, La (Fe, Si)₁₃ phase, magnetocaloric effect

1 Introduction

In recent research, La-Fe-Si alloys with giant magnetocaloric effect are the most promising magnetic refrigerant because of cheap raw materials and environmentally-friendly constituting elements. However, La-Fe-Si magnetocaloric alloys are faced with problems in fabrication. Days of high temperature annealing is needed because nearly none of NaZn₁₃-type La (Fe,

Si)₁₃ single-phase can be obtained through conventional casting. The as-casting will only bring about a constitution of α -Fe phase and LaFeSi phase. Some rapid solidification methods have been adopted to reduce the annealing time [1,2,3]. These methods will reduce the annealing time to 12 hours at most. However, there is no bulk casting methods reported to produce La (Fe, Si)₁₃ phase during solidification. In this work, we adopt the zone melting liquid metal cooling (ZMLMC) directional solidification and increase the volume fraction of the La (Fe, Si)₁₃ phase greatly in La-Fe-Si bulk casting.

2 Experimental

LaFe_{11.6}Si_{1.4} polycrystalline ingots were arc-melted six times using raw materials lanthanum (99.5%) iron (99.99%) and silicon (99.9999%). To prevent volatilization, 5% extra lanthanum was added for as-cast buttons. The button was remelted and followed by a suction casting in chilled cooper molds to get a rod with a diameter of 7.0mm. After polished and cleaned, the rod was remelted again by high-frequency induction in a homemade vacuum ($\sim 10^{-3}$ Pa) ZMLMC furnace. And then, the rod is directionally grown in an alumina crucible (**Figure 1**). The temperature gradient at the solid-liquid interface front can be estimated by [4]:

$$G_{Solid} \approx G_{Liquid} = \frac{T_{Melt} - T_0}{L}$$

The longitudinal section directionally-solidified sample and the as-cast sample are prepared. The microstructure was observed in backscattered electron (BSE) mode by a scanning electron microscope (SEM; Phenom ProX). The composition of the major phases was detected by energy-dispersive spectroscopy (EDS). The crystal structure was characterized using X-ray diffraction (XRD; Rigaku, Ultima IV) using Cu K _{α} radiation at a scan speed of 5°/min.

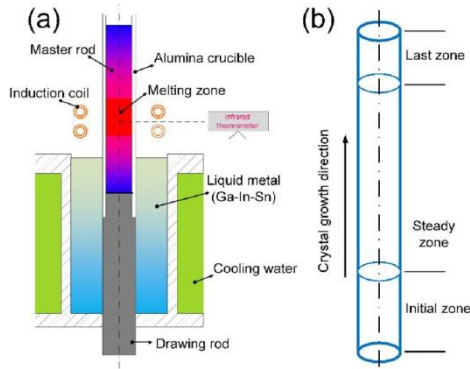


Figure 1. Schematic of the ZMLMC directional solidification furnace (a) and crystal growth along the rod (b).

3 Result and discussion

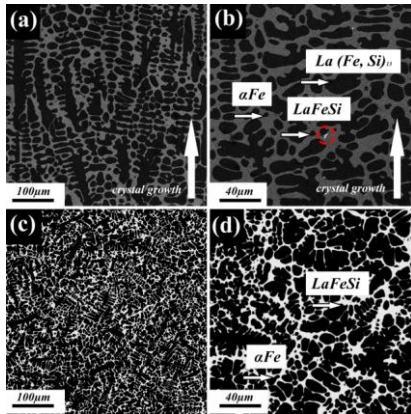


Figure 2. (a) SEM backscattered electron image of directionally-solidified LaFe_{11.6}Si_{1.4}. (b) SEM backscattered electron image of as-cast LaFe_{11.6}Si_{1.4}. (c) and (d) is the amplified image of (a) and (b).

Figure 2(a) and 2(b) show the microstructure and morphology of directionally-solidified LaFe_{11.6}Si_{1.4}. As the figure shows, black phase is α-Fe, grey phase is La(Fe, Si)₁₃ and black phase is LaFeSi. It can be clearly seen that prime α-Fe phase displays a thick and long dendrite microstructure and La(Fe, Si)₁₃ exists within the dendrites. The volume fraction of La(Fe, Si)₁₃ phase is about 30.5% phase. In comparison, as-cast LaFe_{11.6}Si_{1.4} sample is revealed as Figure 2(c) and 2(d).

The XRD patterns for directionally-solidified sample and as-cast samples are shown in Figure 3. NaZn₁₃-type La(Fe, Si)₁₃ phase is confirmed in directionally-solidified LaFe_{11.6}Si_{1.4}. Specially, the La(Fe, Si)₁₃ has two typical crystal structures originating from Si concentration, that is cubic NaZn₁₃-type and tetragonal Ce₂Ni₁₇Si₉-type. To our knowledge, NaZn₁₃-type La(Fe, Si)₁₃ phase demonstrates giant magnetocaloric effect. So

it's meaningful to clarify the crystal structure of La(Fe, Si)₁₃ for practice use.

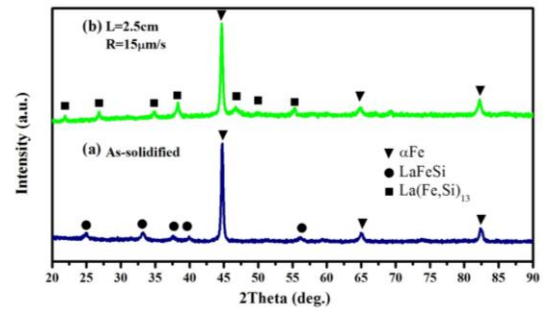


Figure 3. XRD patterns of as-solidified LaFe_{11.6}Si_{1.4} (a) and directionally-solidified LaFe_{11.6}Si_{1.4} (b).

EDS has observed a distinct composition segregation in the La(Fe, Si)₁₃ phase, of which the Si content is about 20.3% much higher than the predicted value. In this case, the real chemical composition of La(Fe, Si)₁₃ phase is La_{6.7}Fe₇₃Si_{20.3}. Previous research [2] has shown that the annealed bulk alloy usually has lower Si content than expected. Our work indicates that Si can dissolve much more by directional solidification.

4 Conclusion

In this work, the volume fraction of La(Fe, Si)₁₃ phase is greatly increased in La-Fe-Si magnetocaloric alloy by ZMLMC directional solidification. Besides, the grain size of the prime phase α-Fe has been increased as well. The element composition segregation is observed and directional solidification can dissolve more Si into La(Fe, Si)₁₃ phase.

5 Acknowledgement

This work is sponsored by National Natural Science Foundation of China (Grant No. 51404152), Shanghai Pujiang Program (Grant No. 14PJ1404800), Shanghai International Cooperation Project (Grant No. 14140711000), and National Basic Research Program of China under contract No. 2011CB012900.

Reference

- [1] Jian Liu, Pengna Zhang, Fuping Daid and Aru Yana. Scripta Materialia 69, 485 (2013).
- [2] O. Gutfleisch, A. Yan, and K. H. Müller. Journal of Applied Physics 97, 10M305 (2005).
- [3] J.D. Dong, A.R. Yan, and J. Liu. Journal of Magnetism and Magnetic Materials 357, 73 (2014).
- [4] Y.J. Huang, Q.D. Hua, J. Liu, L. Zeng, D.F. Zhang, and J.G. Li. Acta Materialia 61, 5702 (2013).

Fabrication of Heterostructure of 3-D Photonic Crystals of Polystyrene Microspheres by Self-Assembly Routes

Doris Liao¹, Martin Tsai¹, Karsa Tsai¹, Jennifer Tsai², M. Srinivas Reddy³, R. Vijaya³, and R.F. Louh¹

¹Dept. of Materials Sci. and Engr., Feng Chia University, Taichung, Taiwan 40724

²Dept. of Photonics, Feng Chia University, Taichung, Taiwan 40724

³Dept. of Physics, Indian Institute of Technology Kanpur, Kanpur 208016, India

Abstract

The monodispersed, narrowly size-distributed polystyrene (PS) microspheres of various diameters were produced by both dispersion polymerization process and emulsifier-free polymerization processes. Subsequently the photonic crystals (PhCs) of PS microspheres upon the ITO glasses and ITO/PET flexible substrates were perfectly formed via electrophoretic self-assembly (EPSA) route and isothermal heating evaporation-induced self-assembly (IHEISA) method. Moreover a swift combination of EPSA and IHEISA technique were employed to fabricate the heterostructure (HS) of PhCs, of which the optical properties were characterized accordingly. The results indicated that the HS of 3-D PhCs templates with two different sizes of PS microspheres, which has multi-photonic band gaps, were fabricated via EPSA and IHEISA technique. The goal of this study is to offer a handy way for developing advanced optical functionalities with enhancement of PBG efficiency.

Keywords: dispersion polymerization, emulsifier-free polymerization, photonic crystals (PhCs), electrophoretic self-assembly (EPSA), isothermal heating evaporation induced self-assembly (IHEISA), heterostructure, polystyrene (PS) microspheres.

1. Introduction

Generally speaking, the photonic crystal (PhC) or colloid crystal materials are consisted of two kinds of constituents with different permittivities built into a periodical structure, e.g. the dielectric matrix with periodic pattern of air voids, in which the incident electromagnetic waves would have the interference with its reflected waves by rejecting the passage of electromagnetic waves at a certain regime of frequencies, would behave a photonic bandgap (PBG)^[1-2]. It is known that a mode defect band can be created within the PGB when a group of defects are introduced to interrupt the structural periodicity of such a PhC material. The photon activity exists as the frequency of electromagnetic waves can be perfectly coupled with such defect mode. Since the mode defect band resides in the

PGB, the rapid decay of photons occurs when the frequency of photons is deviated from defect mode. Thereby the transmission of light passing through the PhC can be manipulated by these defect modes^[3].

For a popular electrophoretic deposition (EPD) technique, fine particles with viable surface charges in the EPD suspension or colloid are moving towards the electrode with opposite electrical charge under the influence being exerted with an external electrical field. Eventually densely and grown into uniform films or layers are deposited, the EPD process has been put in practice in ceramic industry for many years to manufacture a wide range of ceramic coatings or thick films on selected electrically conductive substrates, e.g. formation of SiO₂ and Al₂O₃ insulation layers, BaTiO₃ ferroelectric thick films, TiO₂ coatings, and the membrane electrodes of solid state fuel cells (SOFCs)^[4]. One of attractive merits of EPD is that the dense and even layers can be easily produced in a rapid, controllable fashion onto a conductive substrates in different geometries. We extended this technique to deposit the monodispersed polystyrene (PS) and oxide (SiO₂, TiO₂, ZnO, In₂O₃, SnO₂) microspheres into a closely packed template with a nicely periodic structure by means of electrophoretic self-assembly (EPSA)^[5-6]. This EPSA route allows us to construct the PhCs of microspheres of different dielectric constants to design and fabricate novel photonic devices with ease through combined actions of self-assembly and surface deposition of round and uniform microspheres of a monodispersed colloid. The EPSA process enables us to form colloidal crystals or photonic crystals to easily form a face-centered closely packed (fcc) structure, known as opal structure.

To this date, numerous examples of man-made photonic crystals are created in 1D, 2D and 3D arrangements with rather spectacular photonic behaviors. It is proposed that the complete PBG phenomenon, which is most desired for design of novel device design of optical integrated circuitry, requires to be associated with 3D PhC material^[7]. The aim of our research work tends to aim the development of a heterostructure in the 3D PhC templates made possible by using either organic (PS or PMMA) or inorganic (SiO₂, TiO₂, ZnO, In₂O₃ or SnO₂) microspheres. Herein two low-cost and simple self-assembly schemes, namely, electrophoretic self-assembly (EPSA) and isothermal heating evaporation-induced self-assembly (IHEISA), were employed to form the heterostructure (HS) of a PhC template with various kinds of PS microspheres (avg. size of 200 nm, 220 nm and 465 nm) to be deposited on the surface of ITO glass and ITO/PET plastic substrates.

2. Experimental

2.1 Synthesis of polystyrene microspheres by emulsion-free route

The emulsion-free technique was used to synthesize polystyrene microspheres with the

following precursor chemicals such as styrene monomer (SM), 2,2,azobis(2-methylpropion amidine) dihydrochloride (AIBA) as protonic type initiator, polyvinylpyrrolidone (PVP) as polymerization reaction stabilizer, and ethanol (99.5% alcohol) as organic solvent and deionized water. Firstly the PVP stabilizer and initiator AIB were fully dissolved in the mixture of ethanol and deionized water, followed by the addition of styrene monomer through a gentle constant stirring in a mild reaction temperature condition for 24 hr to form a single polymeric phase. The PS microsphere product, which was obtained by a centrifugation of white precipitates out of polymerization, was consecutively rinsed by ethanol and deionized water for several times. The characteristics of PS microspheres were examined by field-emission SEM (Hitachi, model S-4800) and zeta potential meter (Malvern, Zetasizer, model Nano Series).

2.2 Cleaning of ITO glass and ITO/PET plastic substrates

It is rather critical to maintain a reasonably good surface quality for both ITO coated glass and ITO/PET plastic substrates by cleaning any possible grease or adhered organic debris in the bath of acetone, ethanol, sodium hydroxide under ultrasonic agitation for 30 min sequentially, followed by the soaking such substrate materials in the mixture of sulfate acid and hydrogen peroxide (ratio of 3:1) for a short period of time, normally around 1 min. Finally the substrates were rinsed with deionized water before placing them in an oven for drying (60°C/24 hr). The purpose of such cleaning procedures is to switch the hydrophobicity of substrate surface into hydrophilicity in order to achieve a better surface adhesion capability to secure a better deposition of ordered PhC structure throughout the self-assembly process.

2.3 Formation of self-assembled PhC on ITO substrate by EPSA

Prior to the execution of EPSA process, different batches of PS microspheres were mixed in ethanol-water solvent with various volume ratios in order to create stable colloid for EPSA by ultrasonic agitation for 30 min at least. An external electrical field applied between platinum coated cylinder as counter electrode and ITO glass as working electrode was set under a constant voltage mode for EPSA process. For the same deposition duration, the constrained ordered packing of monodispersed PS microspheres to be deposited as 3D layered PhC templates by simply adjusting electrical field strengths. The morphology and microstructure of PhC templates were examined under field-emission SEM (Hitachi, model S-4800).

2.4 Formation of self-assembled PhC on ITO and ITO/PET substrate by IHEISA

Prior to the IHEISA process, distinct batches of PS microspheres were well mixed in ethanol solvent with to create stable colloid by a similar ultrasonic agitation mentioned above. The high relative humidity condition was selected for an acceptable self-assembly action for both ITO glass and ITO/PET plastic substrates at temperature of 50°C such that the construction of 3D PhC template was achieved due to the fact that there was a satisfactory force balance between exertion of capillary force of neighboring spheres and surface tension derived from solvent and substrate for self-assembly effect. The surface tension exerted by solvent surrounded the microspheres made the deposited spheres to be in an aligned ordered fashion with the aid of capillary force between spheres on the surface of substrate.

3. Results and Discussion

3.1 Self-assembled PhC of PS microspheres on ITO substrate by EPSA

(a) Influence of electrical field strength on EPSA performance

After a number of experimental trials, it was found that concentration of 0.1 wt% PS microspheres (avg. diameter of 500 nm) was dissolved in pure ethanol solvent to get a satisfactory dispersivity. Thus we chose the ethanol as major organic solvent to prepare EPSA colloid. The direct current (d.c.) mode was applied to adjust the various electrical field in a range of 80~110 V/cm for the same deposition time of 20 min. The micrographs of Fig. 1 illustrate the morphology of self-assembled PhC materials, in which the lower electrical field (< 100 V/cm) was unable to offer a good electrophoretic mobility within the colloid such that the relatively loose packed template was derived due to an ineffective self-assembly behavior, as shown in Fig. 1(a). The self-assembly effect was evident as shown in Fig. 1 (b) and (c) yet there were some undesired mismatched crevices were present. When the electrical field was sufficiently provided, the achieved self-assembly can be greatly enhanced, as shown in Fig. 1 (d).

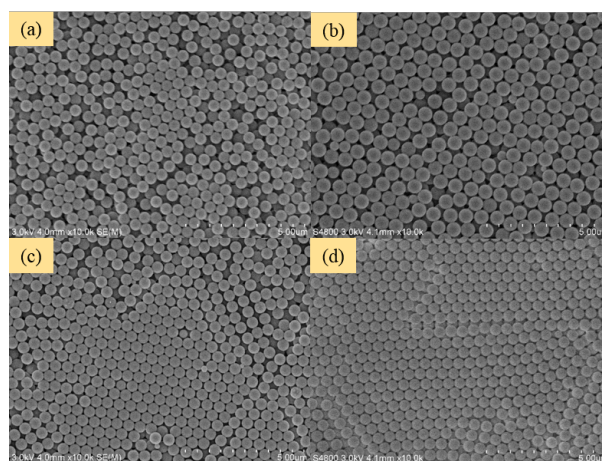


Fig. 1. Top view of self-assembled PhCs under various applied electrical fields: (a) 80 V/cm, (b) 90 V/cm, (c) 100 V/cm, and (d) 110 V/cm, where the deposition time was 20 min.

(b) Building a heterostructure into PhC templates by EPSA effect

Initially we took two kinds of PS spheres (avg. size of 220 nm and 465 nm) to form a heterostructure (HS) by EPSA technique on the surface of ITO glass subsequently, using the d.c. mode, electrical field of 75 V/cm and deposition time of 60 sec. A perfect heterostructure of PS microspheres of two different sizes (220 nm/465 nm) was shown in Fig. 2, along with its reflectance curve of PhC with PS microspheres in a heterostructure, which was further examined by UV-Vis spectroscopy. The number of layers of PhC made of microspheres of different size, either 220 nm or 465 nm, was relatively reduced, as compared to the previous case, as shown in Fig. 1 (d), due to the reduced deposition time was selected. The prerequisite of making the heterostructure in the PhC in this work was in conjunction with a critical thickness, namely the confined number of layers, to maintain the integrity throughout the whole HS to avoid unwanted delamination or layer peeling at any location of PhC by restriction of heavy loading or higher concentration of PS microsphere colloid or a high number of deposited layers for the upper section of heterostructure. Based on this concept, the deposition time during EPSA was then intentionally reduced. Furthermore, the electrical conductivity of ongoing construction of upper portion of HS was somewhat shielded by the lower portion of HS and self-assembly of microspheres at the upper self-assembled portion of HS was slightly interfered to make the number of deposited layers considerably minimized. Currently the number of self-assembled layers was restricted to 3~5 in this case.

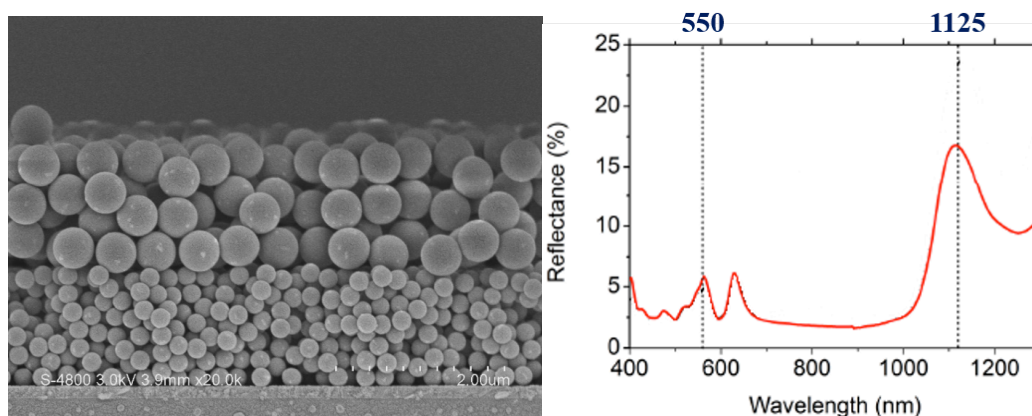


Fig. 2. The heterostructure and reflectance curve of PhC of PS microspheres of two different sizes (220 nm/465 nm).

3.2 Self-assembled PhC of PS microspheres on ITO substrate by IHEISA

The working function of IHEISA, in which there is no requirement to be associated with electrically conductive substrates, is based on maintaining balance of surface tension between solvent and substrate and the capillary force within the solvent to be exerting the neighboring spheres. Herein we tried to form the nicely ordered PhC materials via EPSA and IHEISA for comparing their self-assembly performances. Because most of IHEISA colloids were prepared with ethanol solvent, the evaporation temperature for IHEISA was set at 50°C, which was far below the boiling point of ethanol at 78°C, to avoid to experience a rapid solvent evaporation rate for disrupting the desired self-assembly behavior. Moreover, a higher relative humidity was used to keep evaporation driven surface tension not exceeding the van der Waals force exerting among neighboring spheres, thereby, a better self-assembled PhC template can be expected.

(a) Formation of 3D PhC on ITO glass and ITO/PET plastic substrates

The PhC templates were built from an ethanol-based colloid of 220 nm sized PS spheres on both ITO glass and ITO/PET flexible substrate so that the subsequent microstructural and optical characterization can be smoothly carried out. Figure 3 depicts the morphological results of PhCs on both ITO glass and ITO/PET flexible substrate by IHEISA process. Though the self-assembly was satisfactorily achieved, yet there were few sporadic places with PS spheres scattered on the very top surface of PhC template due to the influence of a local abrupt rapid solvent evaporation. Generally effect of a rapid uncontrollable solvent evaporation would have impact on altering the van der Waals forces among the neighboring spheres so that the continuity and structural integrity of PhC were deteriorate and hampered.

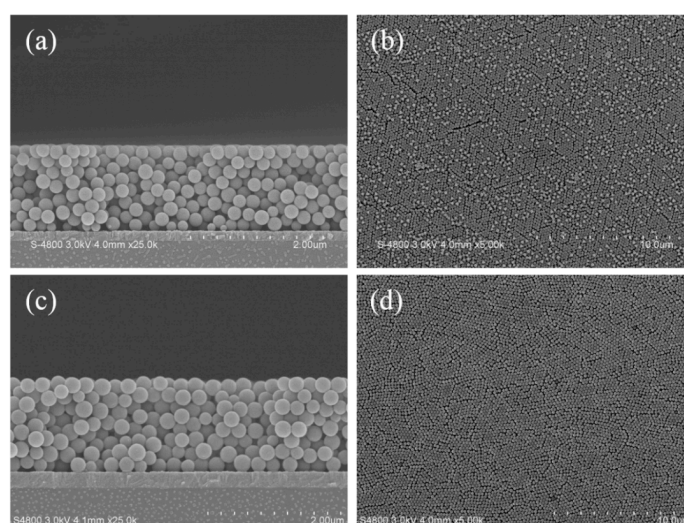


Fig. 3. (a) Cross-sectional view and (b) top view of PhC of 220 nm PS microspheres on ITO glass by IHEISA process, as compared to (c) cross-sectional and (d) top view of similar PhC deposited on ITO/PET plastic substrate.

Since the hydrophilicity of ITO/PET film was relatively poor, the continuity and range of ordered domain of PhC on flexible substrate by IHEISA cannot be obtained satisfactorily. The reflectance of self-assembled sample was manifested by a UV-Vis spectroscopy. The wavelength of theoretical reflectance of PhC with 220 nm spheres is at a peak of 521 nm. However, there is reflectance signal located at 560 nm in Fig. 4, which was delineated from its theoretical value. This result might be speculated for the peak shifting due to the poorly maintained rigidity of flexible substrate during the optical measurement. The ongoing structural improvement by heat treatment or annealing of PhC template as well as their optical measurements are under tested for further validation.

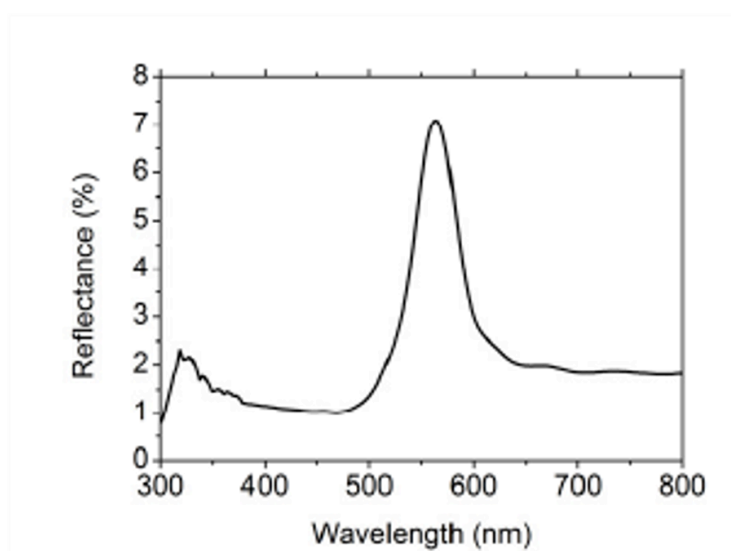


Fig. 4. The reflectance curve of PhC of 220 nm PS microspheres on ITO/PET substrate, which was derived from IHEISA process.

3.3 A heterostructure built into PhC templates by combining EPSA and IHEISA

Based our previous experiences on self-assembly of PS microspheres to construct a heterostructure (HS) into a 3D PhC template by either EPSA or IHEISA route, at this point we tried to manage to attempt the possible synergic effort of combining these two self-assembly schemes above to achieve an improved HS. First of all, the HS was made of lower self-assembled portion of 200 nm spheres by IHEISA and of upper self-assembled portion of 220 nm spheres by EPSA route.

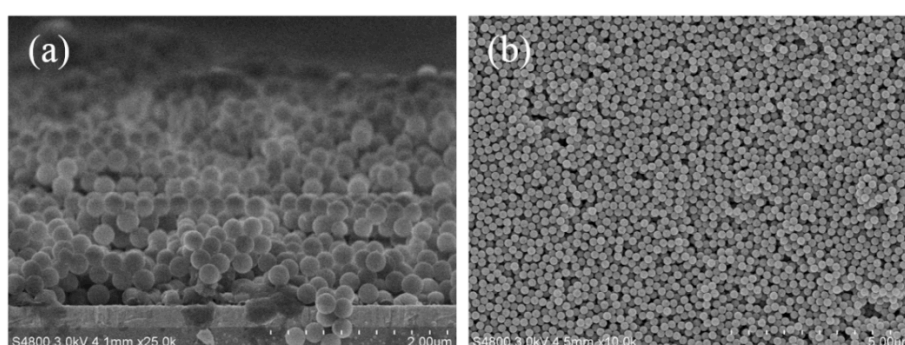


Fig. 5. (a) Cross-sectional view and (b) top view of heterostructure of PhC made of 200 nm (below, by IHEISA) and 220 nm (above, by EPSA) PS microspheres on ITO glass.

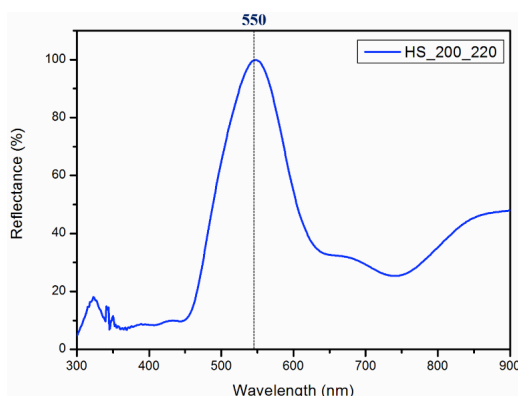


Fig. 6. The reflectance curve of heterostructure of PhC made of 200 nm (below, by IHEISA) and 220 nm (above, by EPSA) PS microspheres on ITO glass.

The microstructure of upper self-assembled portion of HS, as shown in Fig. 5(a), seemed not perfectly attached to the top surface of lower self-assembled portion of HS due to the fact the conductivity between counter-electrode and working electrode was substantially reduced and electrophoretic driving force was adversely affected. Unfortunately, only the limited regions of upper self-assembled portion of HS would present an acceptable structural orderliness, as shown in Fig. 5(b). There is a reflectance peak existing at wavelength of 550 nm in Fig. 6; however, the observed individual characteristic reflection peaks were not sharply corresponding due to the difficulty to obtain a well ordered HS in the PhC in the current study. To overcome such a structural limitation, we have tried to use a different approach by laying the lower self-assembled portion of HS with 220 nm spheres by EPSA, followed by the construction of upper self-assembled portion of HS with 200 nm spheres by IHEISA to obtain an improved heterostructure in 3D PhC template.

The micrograph shown in Fig. 7 illustrates a much sophisticated heterostructure in PhC template consisted of 220 nm (lower portion by EPSA) and 200 nm (top portion by IHEISA) PS microspheres onto the surface of ITO glass. The restricted exertion of electrical field during EPSA was greatly suppressed as well as the limited number of deposited layers of upper portion of HS was successfully acquired by our proposed method, namely the combination of EPSA and IHEISA routes. In addition, the characteristic reflectance peak can be substantially emphasized with current improved scheme.

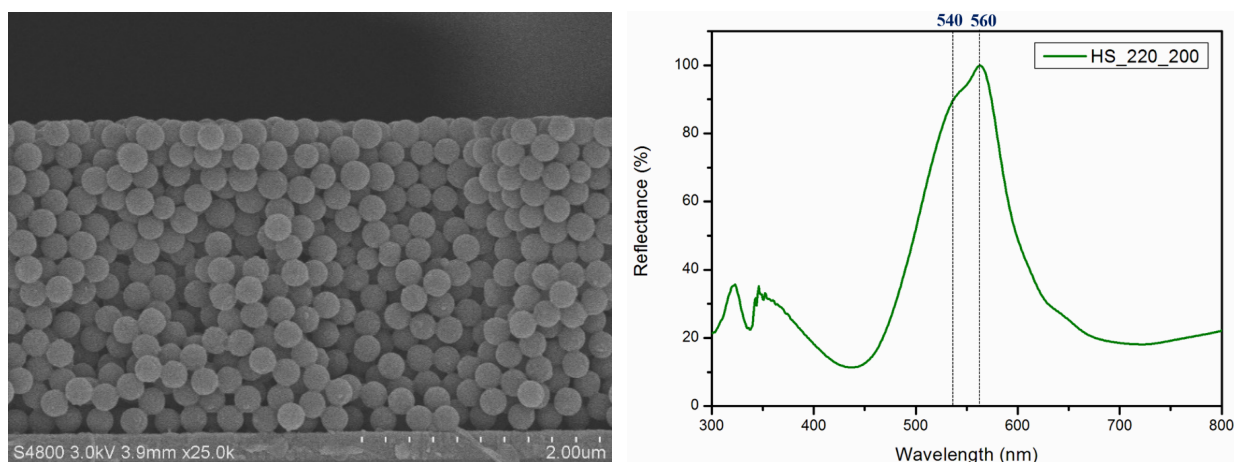


Fig. 7. The cross-sectional micrograph and reflectance curve of heterostructure of PhC made of 220 nm (below by EPSA) and 200 nm (above by IHEISA) PS microspheres on ITO glass.

4. Conclusion

- (1) The positively-charged, monodispersed polystyrene microspheres were successfully produced using emulsion free method coupled with use of protonic type imitator AIBA in an ambient condition. Interestingly a stable colloid production of monodispersive nature of PS spheres was strongly affected the existence of excessive oxygen during the reaction environment. An ongoing synthetic apparatus design for oxygen elimination is underway to acquire improved quality of PS microsphere.
- (2) The 3D PhC and heterostructure in PhC made of PS microspheres on ITO/PET flexible substrates were successfully achieved by IHEISA route and such a specimen responses distinct reflectance peaks.
- (3) The heterostructure of microspheres of two different sizes can be built into a 3D PhC of opal structure by using a synergic process of EPSA and IHEISA. The novel design of resonance micro-cavity or waveguide in conjunction with such PhCs and heterostructures are of great application potential by introduction of particular pattern of clustered defects or line defect.

Acknowledgements

The authors would thank for the grant and supports of this research work from the Ministry of Science and Technology of Taiwan, the Republic of China, under project contracts No. NSC 104-2221-E-035 -017 and No. NSC 103-2923-E-035 -002 -MY3.

References

1. Y. Xia, B. Gates and Z. Y. Li, "Self-assembly approaches to three-dimensional photonic crystals," *Adv. Mater.*, 13 (2001) 409-413.
2. A. J. Turberfield, "Photonic crystals made by holographic lithography," *Mater. Res. Bulletin*, 26 (2001) 632-636.
3. Leo Chau-Kuang Liao, Yuan-Pei Chen, "Effects of voltage operating strategy on electrophoretic self-assembly deposition of spherical SiO₂ particles in water" *Aspects* 429 (2013) 121– 128
4. Yu-Wei Liu, Sumita Pennathur, Carl D. Meinhart , "Electrophoretic mobility of spherical particles in bounded domain" *Journal of Colloid and Interface Science* 461 (2016) 32–38
5. S. Hayashi, Y. Kumanoto, T. Suzuki, and T. Hirai, "Imaging by polystyrene latex particles," *J. Colloid Interface Sci.*, 144 (1991) 538-547.
6. P.H. Wiersema, A.L. Loeb, and J. TH. G. Overbeek, "Calculation of the Electrophoretic Mobility of a Spherical Colloid Particle," *J Colloid and Interface Science* 9 [2] 78~99 (1966)
7. T. Alfrey, E. B. Bradford, and J. W. Vanderhoff, "Optical properties of uniform particle-size latexes," *J. Opt. Soc. Am.*, 44 (1954) 603-609.

Dry ice blasting as a substitution for conventional electroplating pre-treatment processes

Eckart Uhlmann,¹ El Mustapha Baira,¹ Robert Jaczkowski¹

¹Institute for Machine Tools and Factory Management, Technische Universität Berlin, Berlin, Germany

Abstract: For high quality electroplated products, surfaces must be thoroughly pre-treated. For this purpose electroplating currently needs a variety of chemical baths. The used chemicals are injurious to health and harmful to the environment. In addition, the conventional pre-treatment has a long process time which results in high costs. Dry ice blasting alone or in combination with other processes has the potential to completely substitute these conventional pre-treatment processes.

Three process sequences as pre-treatment methods prior to electroplating were investigated on the aluminium alloys AlSi12 and AlMg3. The used processes are dry ice blasting, tempering during dry ice blasting and glass bead blasting followed by dry ice blasting. The influence of the parameters on the surface roughness, surface topography and surface tension of the workpieces was examined. A model to describe the correlation between the dry ice blasting parameters and surface parameters was developed. Finally, an adhesion test of electroplated test specimen was conducted in order to determine the suitability of these alternative pre-treatment processes.

Keywords: Coating; Electroplating; Surface analysis; Dry ice blasting

1. Introduction

Since the results of the galvanic surface treatment are highly dependent on the pre-treatment steps, no residues of grinding and blasting media should remain in and on the workpiece surface [1,2]. A residue-free cleaning is necessary, in order to ensure a high quality coating. Currently electroplating requires a variety of chemical baths for this purpose. Figure 1 shows a simplified schematic diagram of a conventional galvanic process chain.

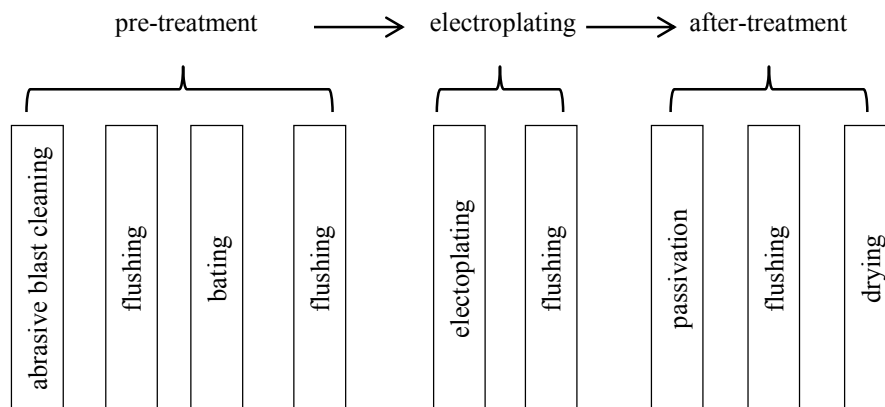


Figure 1: Schematic representation of the electroplating process [3]

2. Materials and methods

To determine the influence of the alternative pre-treatment methods on the roughness, topography and polar component of the surface tension of the workpieces AlSi12 and AlMg3 a Central Composite Design (CCD) was used [4]. With it linear and quadratic interrelation between the setting parameters and the target values can be defined. The dry ice blasting was undertaken with an IceBlast KG 30 Professional system from Ice Tech. Table 1 shows the ranges of the setting parameters by dry ice blasting.

Table 1: Ranges of the setting parameters by dry ice blasting

Setting parameters	Working distance a_p [mm]	Mass flow rate \dot{m} [kg/h]	Jet pressure p_{st} [bar]	Jet angle α [°]	Feed velocity v_f [m/s]
ranges	50 to 100	35 to 65	6 to 10	50 to 80	0.005 to 0.015

3. Results

The following section presents the influence of the alternative pre-treatment methods on the surface of the tested aluminum alloys AlSi12 and AlMg3. According to state of technology the maximum height of profile Rz, the topography as well as the polar component of the surface tension σ_{SP} have a significant impact on the adhesion of the metal layer.

3.1. Influence of the pre-treatment methods on the roughness Rz of the aluminium alloys

According to the mechanical anchoring model, the adhesion of the subsequent coating gets better with higher surface roughnesses [5,6]. Figure 2 shows the three highest achieved roughnesses Rz after the treatment with dry ice blasting, tempering during dry ice blasting and glass bead blasting followed by dry ice blasting. All three pre-treatment methods increased the roughness of the AlSi12-workpieces. The maximum height of profile Rz of an untreated AlSi12-workpiece was $Rz = 2.78 \mu\text{m}$, dry ice blasting increased it to $Rz = 43.26 \mu\text{m}$, tempering during dry ice blasting to $Rz = 49.46 \mu\text{m}$ and glass bead blasting with following dry ice blasting produced the highest roughness of $Rz = 76.22 \mu\text{m}$. AlMg3 has an original roughness of $Rz = 2.55 \mu\text{m}$. Dry ice blasting increased it only to $Rz = 9.30 \mu\text{m}$, tempering during dry ice blasting to $Rz = 40.75 \mu\text{m}$ and the highest roughness was also achieved by glass bead blasting with following dry ice blasting up to $Rz = 85.51 \mu\text{m}$. So, as expected glass bead blasting produced the highest roughness of both aluminium alloys. Additionally, the roughness can be increased by lowering feed velocity v_f of the blasting process.

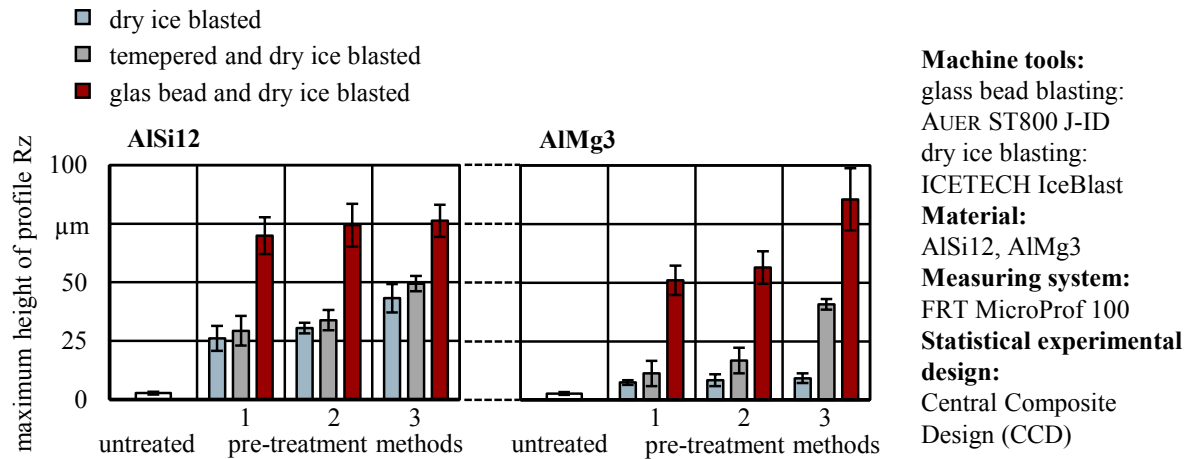


Figure 2: Exemplary results of the roughness of AlSi12- and AlMg3-workpieces after alternative pre-treatment

3.2. Influence of the pre-treatment methods on topography of the aluminium alloys

Dry ice blasting and tempering to 50°C during dry ice blasting lead to a change of the topography of the AlSi12-workpieces. On the other hand these two methods almost did not change the topography of the AlMg3-workpieces. Glass bead blasting with following dry ice blasting changed the topography of both aluminium alloys which resulted in visible impact craters, shown in Figure 3.

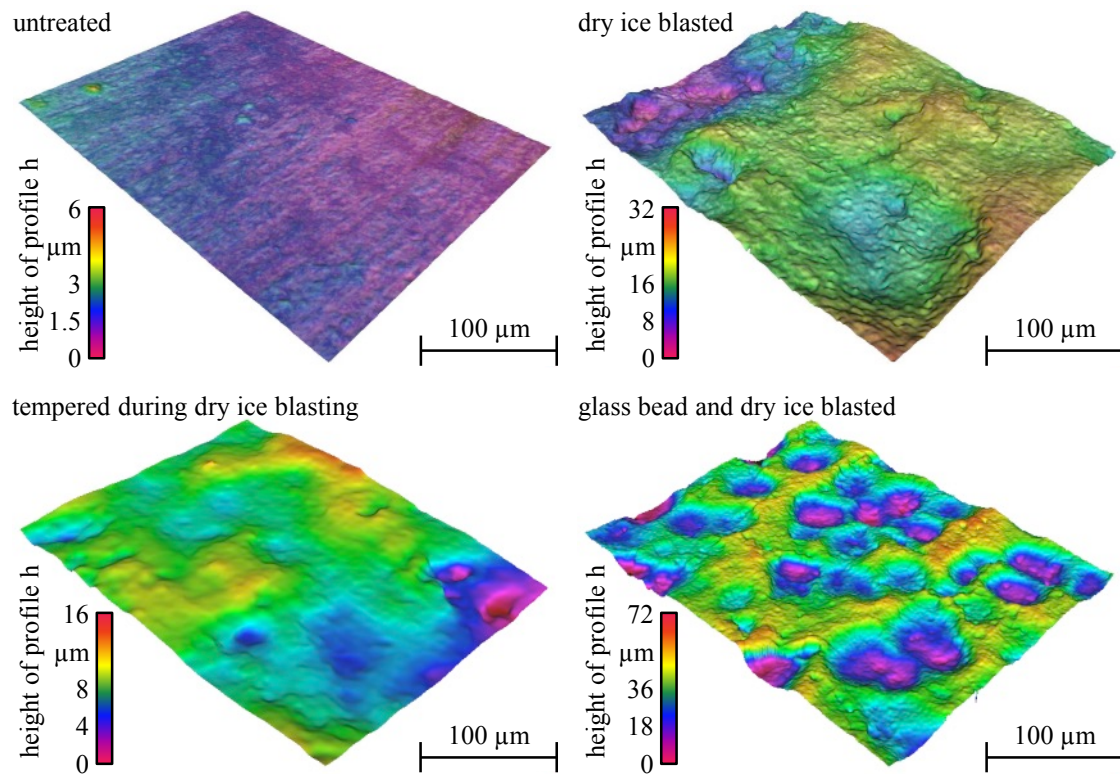


Figure 3: Topography images of AlSi12-workpieces

3.3. Influence of the pre-treatment methods on the polar component of the surface tension of the aluminium alloys

Previous investigations have shown that better adhesion strength can be achieved with high polar component of the surface tension σ_{SP} [6,7]. The surface tension can therefore be used as an indicator for the adhesion strength of the electrodeposited coatings. Only tempering during dry ice blasting increased the polar component of the surface tension σ_{SP} of the AlSi12-workpieces from $\sigma_{SP} = 10.26$ mN/m to $\sigma_{SP} = 37.49$ mN/m, which implies a heterogeneous wetting of the substrate. The polar component of the surface tension of AlMg3-workpieces was increased by all three pre-treatment methods. So the fluid penetrates the more hydrophilic surface (Wenzel-model). Tempering during dry ice blasting produced the highest polar component of the surface tension with $\sigma_{SP} = 43.44$ mN/m

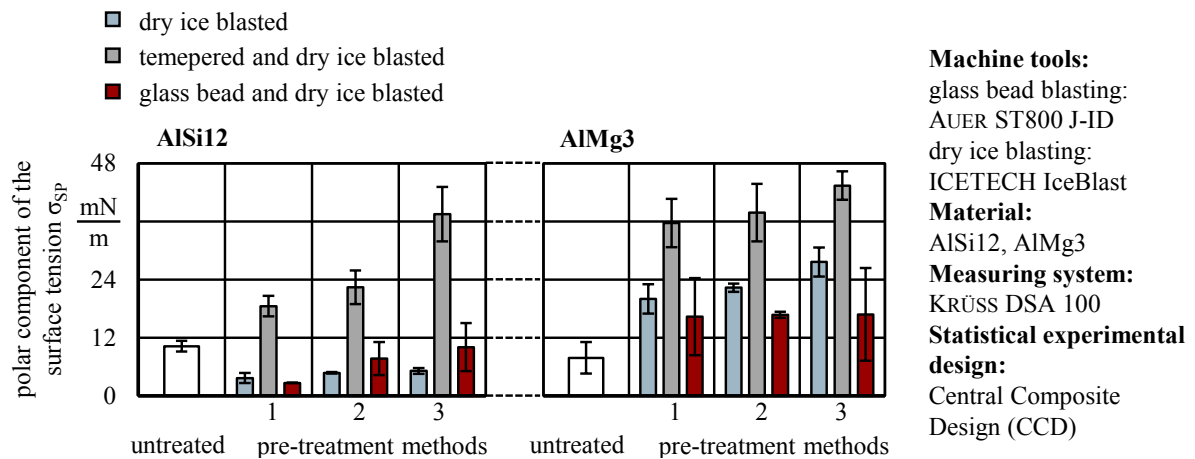


Figure 4: Exemplary results of polar component of the surface tension of AlSi12- and AlMg3-workpieces after alternative pre-treatment

3.4. Adhesion test after electroplating of the aluminium alloys

After the electroplating process the cross cutting index was used as an indicator for the adhesion of the electroplating coat. The cross cutting index between 0 and 2 means that the adhesion was good and the cross cutting index ≥ 3 means that the adhesion was insufficient. Dry ice blasting and tempering during dry ice blasting result in good adhesion (cross cutting index between 0 and 2) with 50 % of the AlSi12-workpieces. After glass bead

blasting with following dry ice blasting almost 90 % of the workpieces were successfully electroplated. 50 % of the AlMg3-workpieces achieved good adhesion after glass bead blasting with following dry ice blasting, Figure 5.

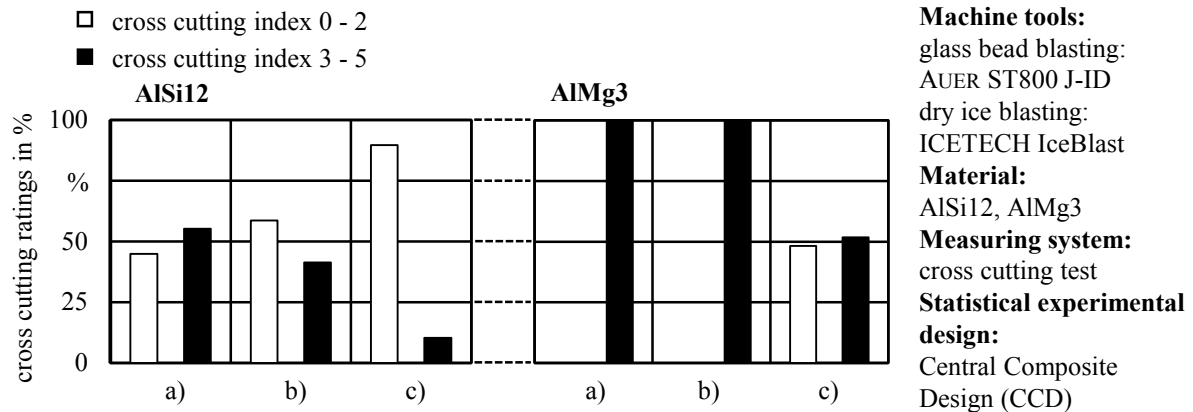


Figure 5: Cross cutting ratings of AlSi12 and AlMg3: a) after dry ice blasting, b) after tempering during dry ice blasting, c) after glass bead blasting with following dry ice blasting

4. Discussion

It was found that the polar component of the surface tension has no significant effect on the adhesion of the electroplated layers. The roughness and the surface topography however have a significant influence on the adhesion after the electroplating. With dry ice blasting a successful electroplating of AlSi12 samples was achieved. Based on the entire investigations, the pre-treatment with dry ice blasting is considered to be a suitable substitution to other pre-treatment methods in order to further enhance the adhesive strength.

5. Acknowledgements

This paper is based on results acquired in the project DFG UH 100/154-1, which is kindly supported by the German Research Foundation (DFG). Furthermore the author would like to thank the company which participated in this research project.

References

- [1] E. Uhlmann, E. M. Baira, M. Kretzschmar, Trockeneis statt Beizen, Journal für Oberflächentechnik (JOT), (2013) 60-63.
- [2] H. Narcus, Metallizing of plastics, Reinhold Publishing Corp., New York, 1960.
- [3] T. W. Jelinek, Praktische Galvanotechnik, in: Eugen G. Leuze Verlag, 7. Auflage, Bad Saulgau, 2013.
- [4] R. J. Del Vecchio, Design of Experiments, Carl Hanser Verlag, München, 1997.
- [5] R. Suchentrunk et al., Kunststoff-Metallisierung. Bad Saulgau: Eugen G. Leuze, 2007.
- [6] W. Brockmann, Haftung als Basis für Stoffverbunde und Verbundwerkstoffe. Hrsg.: Deutsche Gesellschaft für Metallkunde e.V., 1990.
- [7] H. Gleich, Zusammenhang zwischen Oberflächenenergie und Adhäsionsvermögen von Polymerwerkstoffen am Beispiel von PP und PBT und deren Beeinflussung durch die Niederdruck-Plasmatechnologie. Dissertation, Universität Duisburg-Essen, 2004.
- [8] T. Hühns, Charakterisierung und Auslegung der Grenzschicht PVD-beschichteter Schneidkeramiken. In: Uhlmann, E. (Hrsg.), Berichte aus dem Produktionstechnischen Zentrum Berlin. Fraunhofer-Verlag: Stuttgart, 2010.

Figures

Figure 1: Schematic representation of the electroplating process [3]

Figure 2: Exemplary results of the roughness of AlSi12- and AlMg3-workpieces after alternative pre-treatment

Figure 3: Topography images of AlSi12-workpieces

Figure 4: Exemplary results of polar component of the surface tension of AlSi12- and AlMg3-workpieces after alternative pre-treatment

Figure 5: Cross cutting ratings of AlSi12 and AlMg3: a) after dry ice blasting, b) after tempering during dry ice blasting, c) after glass bead blasting with following dry ice blasting

Tables

Table 1: Ranges of the setting parameters by dry ice blasting

Ni-Ti Shape Memory Alloy Sheet Part Stretch Formed at Room Temperature

K.-J. Fann,^{1,*} J.-Y. Su¹

¹Department of Mechanical Engineering, National Chung Hsing University, Taichung, Taiwan

*kjfann@nchu.edu.tw

Abstract:

Because of its superior properties in shape memory effect and superelasticity by changing temperature to have a transformation between its martensitic and austenitic phases, the shape memory alloys can serve as smart materials in transducer and sensor applications. Most of Ni-Ti alloys, which are the most used shape memory alloys, are in austenite phase at room temperature, showing high strength and being hard to deform. To easily form Ni-Ti shape memory alloy sheets, they conventionally are formed and constrained in die sets at an elevated temperature, which is tool-consuming and therefore becomes a cost intensive process. To reduce the investment in capital, this study tried to use the die set only to form the Ni-Ti shape memory alloy sheets at room temperature. No further die set is used in the subsequent heat treatments. In this study, a round Ni-rich Ni-Ti shape memory alloy sheet was solid solved at 800°C, stretched in different strokes by a hemispherical punch at room temperature, and followed with an aging process at 300°C for shape memory treatment. As a result, for smaller punch strokes the sheets could not be well formed, because the maximum strain presented in the alloy was little bit over the elastic region. After the aging process, the heights of the formed sheets were slightly shortened because of a further springback. However, if the sheet part was immersed in liquid nitrogen basin to have its martensitic phase and compressed into a flat shape, the original shape of the part can be fully recovered by returning to room temperature.

Keywords:

shape memory alloy, shape memory effect, Ni-Ti shape memory alloy, stretch forming, cold forming, free recovery.

Introduction:

The conventional process to form shape memory alloys into shapes and have them possess shape memory effect is to form the alloys with a pair of dies in hot state, keep the alloys and the dies in a constraint state inside a heat treatment furnace to develop the shape memory effect by aging, and then quench the alloys in a water basin [1]. To reduce the use of expensive die sets in the forming and the constraint aging process at elevated temperature, it might be worthwhile to try forming the shape memory alloys at room temperature in order to see their form accuracy and shape memory effect in cold state and after the subsequent heat treatment without additional dies [2]. This study is thus aimed to inves-

tigate the feasibility of the above proposed processes for shape memory alloy sheet part: cold forming with only one die set and aging without any further die set.

Setups:

In this study, a commercially acquired Ni-rich (50.0~50.8at% Ni) Ni-Ti shape memory alloy sheet having the thickness of 0.9 mm was cut in the shape of a circle with a diameter of 36 mm and placed in a heated chamber at 800°C for one hour and then quenched in water, which served as a solid solution process affiliated to an annealing process. This sheet blank was then stretch formed with a hemispherical punch of 30 mm in diameter to a stroke 1 mm, 2 mm, 3 mm, and 4 mm, respectively. Figure 1 shows the schematic setup and the apparatus for the cold stretch forming process. For each stroke a separate bottom die is equipped. The forming process is executed in a universal testing machine.

After removing the punch, the formed part was then put into a furnace for aging treatment at 300°C for one hour and subsequently quenched in water. The shape memory effect of the stretch formed parts was investigated as well by checking the height of the sheet parts recovered by returning temperature to the austenitic phase completely presented after compressing them into a flat shape at a temperature, at which the martensitic phase is completely presented.

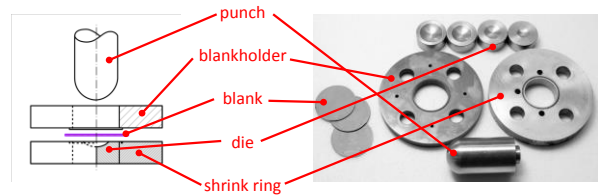


Figure 1: experiment setup.

Results and Discussion:

Figure 2 shows the stress-strain diagram of the at 800°C solid-solved Ni-Ti shape memory alloy sheet in a tensile test at room temperature. The shape memory alloy shows a large linear elastic strain range around 3% and has no evident necking before fracture but still shows a large ductile strain over 20%. Because the sheet has its austenitic phase at room temperature, it is hard to deform and shows a strong strain hardening effect.

Figure 3 shows the punch load to the sheet blanks in the different forming strokes at room temperature. The punch load during downward stroke was higher than that during upward stroke, because there was

plastic deformation downwards whereas only elastic springback. The springback was relatively high and its load vs stroke curve was not linear either. The load was almost fully recovered at the early upward stroke but for the latter stroke upwards the load decayed very slowly. It also shows the hysteresis. The larger the area enclosed, the more the plastic deformation and the better the form precision. As shown in Figure 3, the higher the punch stroke, the larger is the area and therefore it is expected that the less the springback and the more precise the part formed. The curves for downward and upward stroke almost overlap each other for the forming stroke of 1 mm. It means that the formed geometry almost sprang back to flat shape, which can be observed in Figure 4. The part for the forming stroke of 2 mm is also hard to see the formed shape.

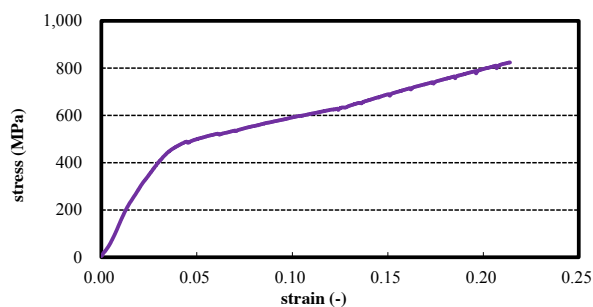


Figure 2: Stress vs strain of Ni-Ti shape memory alloy sheet in tensile test.

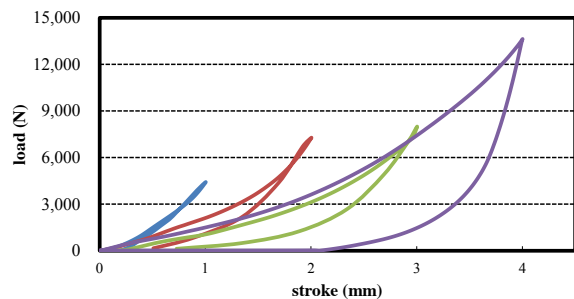


Figure 3: Load vs stroke during stretch forming under different strokes.

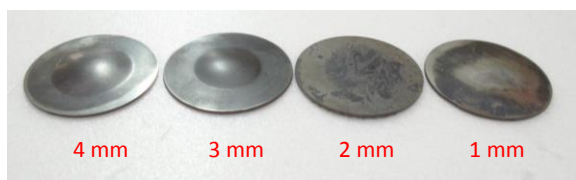


Figure 4: Stretch formed shape memory alloy parts under different strokes.

It shows as well in Figure 3, that the punch load for the lower stroke was always higher than that for the higher stroke while the punch was at the same stroke. It can be attributed to that the blank was clamped by the blankholder and the bead on the blankholder bit the blank before the forming stroke to restrict the

material of the blank from the flange on the blankholder into the die cavity, so that it needed more force to form the blank.

At room temperature, all the formed and subsequently aged parts had their austenitic phase and demonstrated a shape memory effect as well after a compression to the flat shape in a liquid nitrogen basin, in which the temperature is lower than -196°C and the martensitic phase is fully presented in the parts. Figure 5 shows that all the flattened parts almost recovered their formed shapes after returning to room temperature.

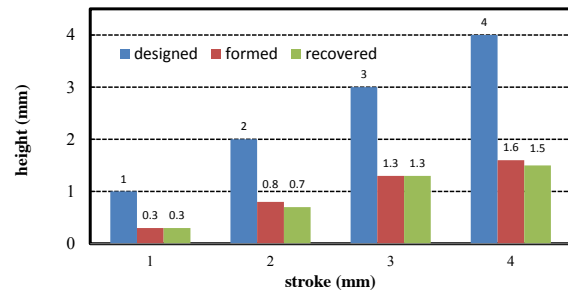


Figure 5: Height recovered after compressing the part to a flat shape.

Conclusions:

It can be concluded that the process proposed by this study – to stretch form a shape memory alloy sheet at room temperature to have a shape with shape memory effect by means of a solid solution treatment before and an aging treatment after cold forming – is feasible. The springback after stretch forming and during aging can be compensated by modifying the punch radius, so that a tolerable shape with shape memory effect can be achieved with only one die set. It might be investigated how the sheet parts undergo a constrained recovery by clamping them in a liquid nitrogen basin and returning to the room temperature.

Acknowledgements:

The authors would like to thank Ministry of Science and Technology of Republic of China for financial supporting this research under the grant MOST 104-2221-E-005-022.

References:

- [1] Duerig, T.W., Melton, K.N., Stoeckel, D., Wayman, C.M. (1990), *Engineering aspects of shape memory Alloys*, London: Butterworth-Heinemann Ltd.
- [2] Fann, K.-J., Huang, P.-M. (2015), Shape memory effect in aging of Ni-Ti shape memory alloy wire bent in V-shape at room temperature, *Proceedings of the Shape Memory and Superelastic Technologies Conference, SMST 2015: The Model for Shape Memory Application, Oxfordshire, UK*.

HEAT TREATED SCANDIUM REINFORCED A356 GRAVITY DIE CAST ALUMINIUM ALLOY

Y. P. Lim^a, W. H. Yeo^b, A. Masita

Department of Mechanical & Material Engineering

Universiti Tunku Abdul Rahman, 53300 Kuala Lumpur, Malaysia

^alimyp@utar.edu.my, ^byeowh@utar.edu.my

Abstract:

The effects of Scandium (Sc) addition (0.00wt%, 0.2wt%, 0.4wt% and 0.6wt%) and T6 heat treatment on the microstructure and mechanical properties of A356 aluminium alloy have been investigated in the present work. The specimens were prepared by gravity die casting process and machined according to ASTM B557-06 standard. The microstructure, microhardness and tensile strength of the cast products were examined by Scanning Electron Microscopy (SEM), Vicker's Hardness Tester and Instron Static Machine respectively. It was found that the grain structure of A356 aluminium alloy had changed from coarse and elongated shape to finer and equiaxed structure and the average grain size was reduced by the addition of scandium. The eutectic morphology was also converted into a finer and fibrous structure through modification of scandium on the eutectic silicon. The addition of scandium from 0.00wt% to 0.4wt% does show the decreasing in average grain size. While increment from 0.4wt% to 0.6wt% of scandium does not show significant reduction in grain size and the difference was only 0.1µm. T6 heat treatment plays an important role in the fragmentation and spheroidization of eutectic silicon, especially in the Sc modified A356 alloy. The tensile properties were improved by the addition of scandium followed by the T6 heat treatment. A great combination of ultimate tensile strength (161.57MPa) and microhardness (118.10 HV) was obtained when the Sc addition was at 0.6wt%.

Keywords: A356; Scandium Effect on Mechanical Properties; Aluminium Alloy; Mechanical properties; Gravity Die Casting;

Introduction

Aluminium and its alloy have good specific mechanical properties of high strength-to-weight ratio, lower price, recyclability, high corrosion resistance and excellent machinability. As referred to S. A. Sajjadi et al¹ aluminium has excellent castability. The application of aluminium alloys has been widely used in automotive, military, aerospace and electrical industry¹. A356 aluminium alloy is one of the most popular aluminium alloys that have been commercialized by the industry nowadays due to its good mechanical properties, castability and corrosion resistance⁴. It is also widely applied in machine manufacturing, aerospace and automobile industries⁴.

In order to fulfil the requirement of service structural aircraft and automobile components, the higher mechanical properties such as tensile, hardness and fatigue are needed. The ability of aluminium alloy with higher resistance at high temperature is also needed. The promising approach that can improve the mechanical properties is by adding another alloying element either with low solubility or totally insoluble in aluminium⁸.

Among the range of possible element, Scandium (Sc) was claimed to be a very potent grain refiner for cast aluminium alloy⁷. Wattanchai et al² reported the inoculation of Scandium in aluminium by has shown the effectiveness to increase the strength, reduce hot tearing susceptibility and increase corrosion resistance. Besides that, they also reported Sc increases the recrystallization temperature of aluminium alloy up to 600°C. S. Costa et al⁸ found that small additions of Sc (up to 0.8wt.%) can improve the aluminium alloys properties including mechanical strength⁸ and modification of eutectic structure from a coarse, plate-like and acicular form to a finely branched and fibrous one⁵. They also revealed that heat treatments with temperature of 250-350°C for Al alloys with up to 1wt% Sc able to promote considerably hardening.

In general, heat treatment is a process for determining casting microstructure and mechanical properties. A356 alloys are made up of coarse primary α -Al dendrites and acicular-shaped eutectic silicon, which affect the mechanical properties and limit its application. Heat treatment process is able to homogenize α -Al dendrites in aluminium alloys⁹. As for T6 heat treatment, it is usually used to improve the fracture toughness and yield strength of aluminium alloy⁶. Peng et al⁶ reported, the factors influencing the efficiency of heat treatment of aluminium alloys are temperature, holding time and alloying addition.

However, a comprehensive study on the effects of heat treatment on the mechanical properties of A356 aluminium alloys with additional of Sc have been less reported in the literatures. Therefore the current work aims to examine the microstructural characterization and investigate the mechanical properties of heat treated A356 with different scandium.

Methodology

Sample Preparation. In this work, four different compositions of scandium were produced by gravity die casting process, namely A356, A356 + 0.2wt% Sc, A356 + 0.4wt% Sc, and A356 + 0.6wt% Sc. The furnace crucible is set at 850°C at the control panel for 90 minutes to fully melt A356 alloy. Then, the Al-2Sc was added to the molten aluminium alloy and the mixture was left 15 minutes for mixing purpose. Manual stirring of the melt was done for a few times to ensure the distribution of Sc is even throughout the melt. Once the mixing process is done, the molten aluminium was poured into the cavity of the pre-heated gravity die casting mould which has the design following as shown in Fig.1.



Fig. 1 Core and cavity of die

Heat Treatment. Four as-cast samples were machined into tension rods. The samples were heat treated in an electrical furnace at 540°C for 8 hours and quenched in warm water at 60°C no longer than 6 seconds. The samples were then naturally aged at room temperature for 20 hours, before being artificially aged at 185°C for 8 hours.

Testing. Surface morphology of the samples was examined using Hitachi VP-SEM S-3400N. EDS analysis was performed in conjunction with SEM examination. The uniaxial tensile test was performed at strain rate of 1mm/min on the Instron 5582 universal testing machine until the specimen fractured. For Vicker's hardness test, the specimens were prepared according to ASTM E384.

Result and Discussion

Microstructure Evaluation. Fig. 2 and Fig. 3 show the SEM result and average grain size of the samples before and after heat treatment process. The data shows that the grain size decreases as the wt% of Scandium increases. These outcomes verify that Sc can affect grain refinement. Juan Ma et al¹⁰ detected the addition of Sc could make the grain size of an alloy reduced and turned to non-dendritic form. However, when the percentage of Sc does exceed the needed amount, the grain size reduction is hardly seen. This is shown in the graph which only a slightly decrease from 0.4 to 0.6 wt% of Sc; while from 0.2 to 0.4 wt%, grain size reduction is significant. S. Costa et al⁸ stated that the formation of a perfect equiaxed structure is due to the precipitation of the Al₃Sc phase, which is the first forming phase from the melt in hypereutectic alloys. The columnar structure is replaced by a fine equiaxed structure throughout the sample. This is extremely importance to the performance of a cast component. The fine and equiaxed grain microstructure has numerous benefits in cast alloys, improving the mechanical properties, distribution of second phase precipitates, reducing shrinkage porosity and improve the achievement of uniform anodized surfaces⁸.

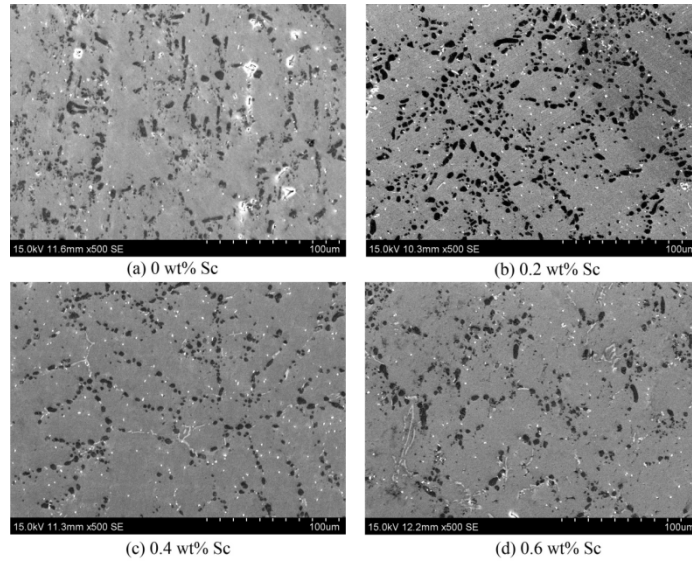


Fig. 2 SEM Micrographs of HT samples (500x)

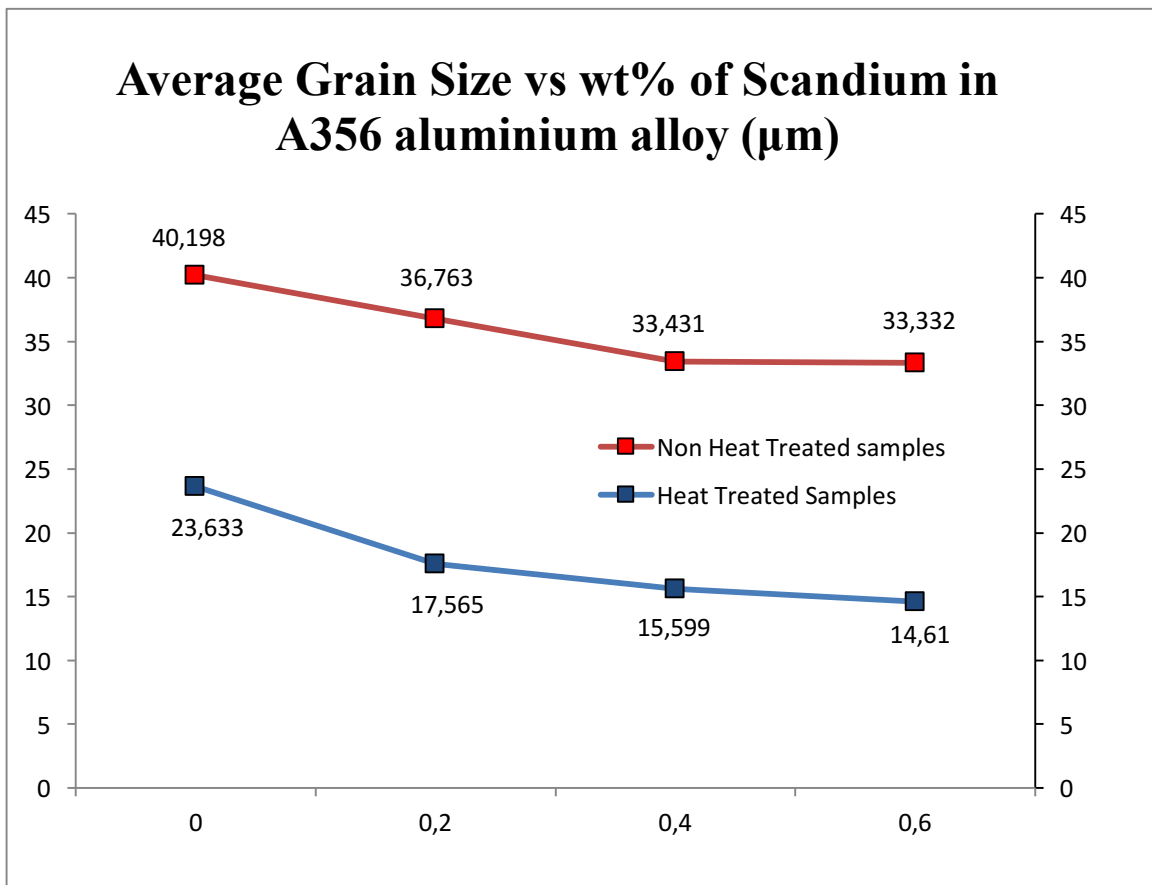


Fig. 3 Graph of Average Grain Size vs wt% of Scandium in A356 aluminium alloy

Tensile Test Evaluation. The result of tensile testing of samples is shown in Fig. 4. The tensile strength increase when the Scandium amount increases. Due to the modification and

refining of the microstructure, tensile strength can be improved until 161.57 MPa by 0.6wt% of Scandium which shows the highest tensile strength among samples. However, 0.4wt% of Scandium has insignificant difference with 0.6wt% of Sc. Penget al⁶ concluded during tensile strain, inhomogeneous deformation in the microstructure induces internal stresses and shows the attraction of the intermetallic particles. Higher value of tensile strength shows higher attraction between the particles. Tensile strength of heat treated samples being compared to non-heat treated samples in Fig 4. The heat treated samples have higher ultimate tensile strength with mean of 25% compared to non-heat treated samples.

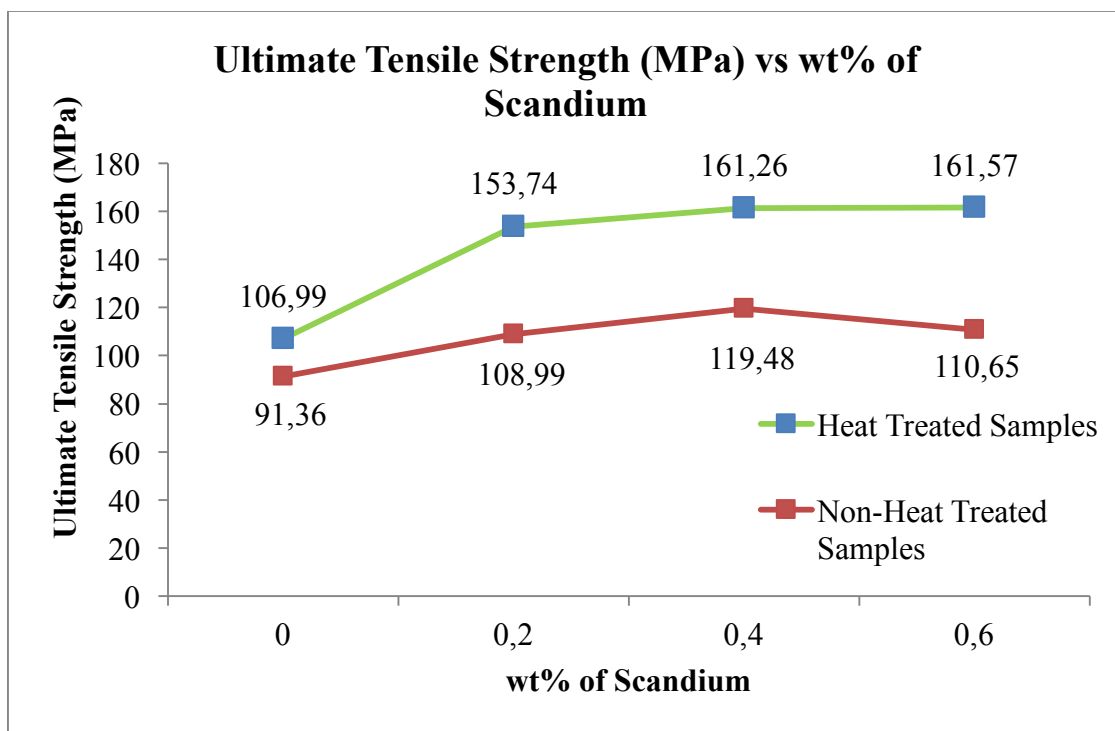


Fig. 4 Graph of Ultimate Tensile Strength (MPa) vs wt% of Scandium in A356 aluminium alloy

Hardness Test Evaluation. Fig. 4 shows the micro hardness of heat treated and non-heat treated samples. The result shows micro-hardness of the samples increase as the Scandium percentage increase. Similar to tensile test result, 0.6wt% Sc sample indicate the highest value of microhardness. Both heat treated and non-heat treated samples shows almost consistent value when the Scandium amount is 0.6wt%. K. T. Akhilet al⁹ reported heat treated samples has lower grain size and cause the microhardness of aluminium alloy has minor difference. It is noticed that the heat treated samples exhibit higher value compared to commercial heat

treated A356, which varied from 88 to 100. Non heat treated samples showed slightly lower reading of microhardness at mean of 6% with same content of Sc.

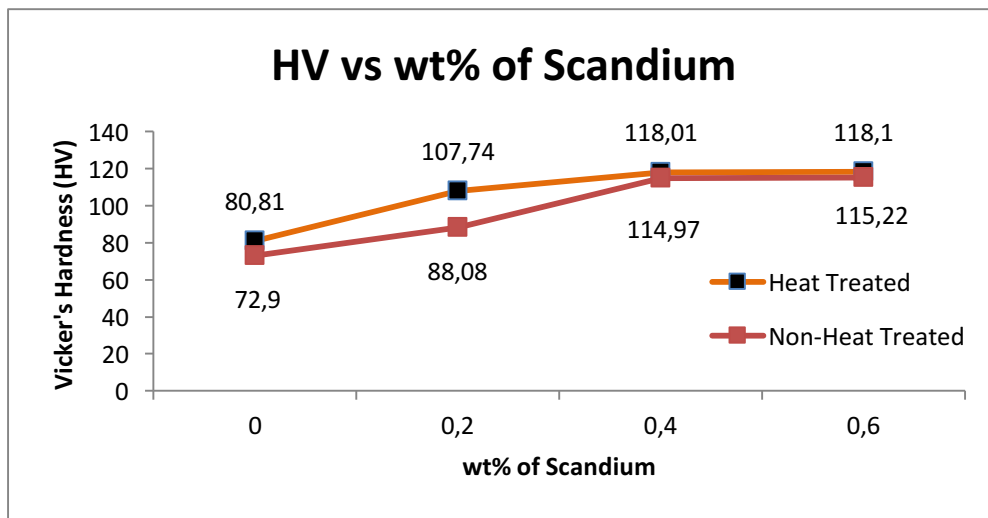


Fig. 4 Vicker's Hardness vs wt% of Scandium in A356 aluminium alloy

Conclusion. In the current research, A356 added with Scandium were fabricated by using gravity die-casting process and effect of the various amount of Scandium on microstructure and mechanical properties were investigated. The following were obtained:

1. The grain size of A356 was refined by Sc, reduced by 8% at 0.2wt% Sc but further increase in Sc wt%, the grain size does not reduce significantly. By applying heat treatment, the grain size of 0.2wt% Sc was reduced by 60% and does not reduce significantly after that.
2. The ultimate tensile strength of 0.2wt% Sc improves 20% and after that no significant improvement. By applying heat treatment, the 0.2wt% Sc achieved 40% improvement but further increment of Scandium does not improve the UTS anymore.
3. The microhardness shows significant improvement of ~50% at 0.4wt% Sc for both non-heat-treated and heat-treated samples.

References

1. S.A. Sajjadi, H.R. Ezatpour, M. TorabiParizi, Comparison of microstructure and mechanical properties of A356 aluminum alloy/ Al_2O_3 composites fabricated by stir and compo-casting processes, *Materials and Design*, 34, (2012)106–111
2. WattanachaiPrukkanon, NakornSrisukhumbowornchai, ChaowalitLimmaneevichitr, Influence of Sc modification on the fluidity of an A356 aluminum alloy, *Journal of Alloys and Compounds*, 487, (2009)453–457

3. S. Menargues, E. Martín, M. T. Baile, J. A. Picas, New short T6 heat treatments for aluminium silicon alloys obtained by semisolid forming, *Materials Science & Engineering, A621*, (2015) 236–242
4. Zhiwei Liu, Xiaoming Wang, Qingyou Han, Jianguo Li, Effects of the addition of Ti powders on the microstructure and mechanical properties of A356 alloy, *Powder Technology*, 253, (2014) 751–756
5. Wenda Zhang, Yun Liu, Jing Yang, Jinzhi Dang, Hong Xu, Zhenmin Du, Effects of Sc content on the microstructure of As-Cast Al-7 wt.%Si alloys, *Materials Characterization*, 66, (2012) 104–110
6. Peng Ji-Hua, Tang Xiao-Long, He Jian-Ting, Xu De-Ying, Effect of heat treatment on microstructure and tensile properties of A356 alloys, *Trans Nonferrous Met. Soc. China*, 21, (2011) 1950–1956
7. M.S. Kaisera, S. Datta, A. Roychowdhury, M.K. Banerjee, Effect of scandium on the microstructure and ageing behaviour of cast Al–6Mg alloy, *Materials Characterization*, 59, (2008) 1661–1666
8. S. Costa, H. Puga, J. Barbosa, A.M.P. Pinto, The effect of Sc additions on the microstructure and age hardening behaviour of as cast Al–Sc alloys, *Materials and Design*, 42, (2012) 347–352
9. K.T. Akhil, Sanjivi Arul, R. Sellamuthu, The Effect of Heat Treatment and Aging Process on Microstructure and Mechanical Properties of A356 Aluminium Alloy Sections in Casting, *Procedia Engineering*, 97, (2014) 1676 – 1682
10. Juan Ma, Desheng Yan, Lijian Rong, Yiyi Li, Effect of Sc addition on microstructure and mechanical properties of 1460 alloy, *Progress in Natural Science: Materials International*, 24, (2014) 13–18
11. Pramod S. L., Prasada Rao A. K., Srinivasa R. Bakshi, Effect of Sc addition on the microstructure and wear properties of A356 alloy and A356-TiB₂ in situ composite, <http://www.researchgate.net/publication/275275451>

Low-temperature plasma modification of fillers for advanced polymer composites

M. Siciński¹, D. Bieliński¹, H. Szymanowski², M. Gazicki-Lipman², A. Sobczyk-Guzenda², T. Gozdek¹

¹Institute of Polymer & Dye Technology, Lodz University of Technology, Stefanowskiego 12/16, 90-924 Lodz,

²Institute of Materials Science and Engineering, Lodz University of Technology, Stefanowskiego 1/15, 90-924 Lodz, Poland .

Introduction:

In polymer industry there still is a room for new fillers, which can improve composites performance or introduce a new function to the material. Modern fillers like carbon nanotubes or graphene nanoplatelets, are more and more often applied in advanced polymer composites technology. Very often it is hard to obtain a well dispersed system for such fillers, as the particles are not wet properly by the polymer during mixing. As a consequence, the total effect of mechanical properties improvement of a composite is lower than expected.

Low-temperature plasma can be observed as a discharge between electrodes in low-pressure reactor chamber. The discharge is maintained in a presence of a process gas, which for example can be Ar₂, O₂, H₂, N₂, acetylene, methane, or simply air. Depending on a type of gas used an controlling of process parameters, plasma treatment can be used for cleaning of the material's surface(so called "micro-sandblasting"), or etching of some functional groups via material's reaction with ionized gas particles. The plasma techniques application possibilities are very promising, especially due to environment protection issues – plasma treatment does not generate waste, is fast, and energetically advantageous process.

In this work multi-walled carbon nanotubes (MWCNT), graphene nanoplatelets (GnP) and carbon fibers surface was modified with low-temperature plasma. Attempts were made to graft some functional groups on plasma-activated material to make filler's surface chemically active during processing. The analysis of surface free energy of virgin and modified fillers was carried out. Ultimately rubber composites were produced, and their mechanical properties were studied.

The scope of work:

1. Modification of filler surface in low-temperature plasma.
2. Estimation of the filler surface free energy with Owens-Wendt method.
3. Production of elastomer composites containing modified fillers.
4. Estimation of composites properties – mechanical tests, micromechanical analysis, dispersion tests, microstructure analysis.

Materials:

1. Multiwalled carbon nanotubes(MWCNT), purity 98% mass, CheapTubes (USA)
2. Graphene nanoplatellets, purity 98% mass, CheapTubes (USA)
3. Carbon fibers KCF-100, Kureha (Japan)
4. Styrene-butadiene rubber KER-1500, Synthos(Poland)
5. Vinyltrimethoxy-silane, 98%, Sigma Aldrich(Germany)

Fillers were modified in low-temperature plasma reactor. Firstly, the surface was activated with oxygen or nitrogen discharge. Subsequently, the chamber was filled with vapours of coupling agent. The conditions of both modification stages varied.

Each material needs an optimization of the modification process due to different chemical and physical properties. Also the polymer matrix where the filler will be incorporated have to be considered. For several samples better mechanical properties of the composites were obtained (tensile strength and elongation at break). It was also observed, that the chemical modification of a filler surface affects the crosslink structure and the dynamic behaviour of the polymer.

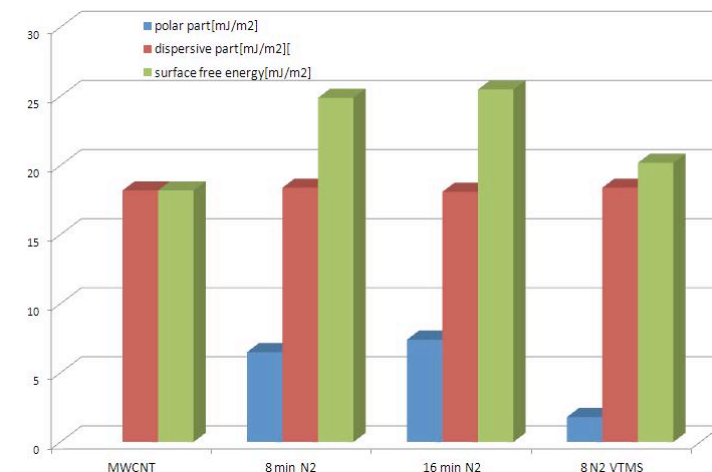


Fig.1 Surface free energy and its parts for virgin and modified multiwalled carbon nanotubes (MWCNT). Modification conditions: plasma power – 100W, time of modification 8 or 16 min.

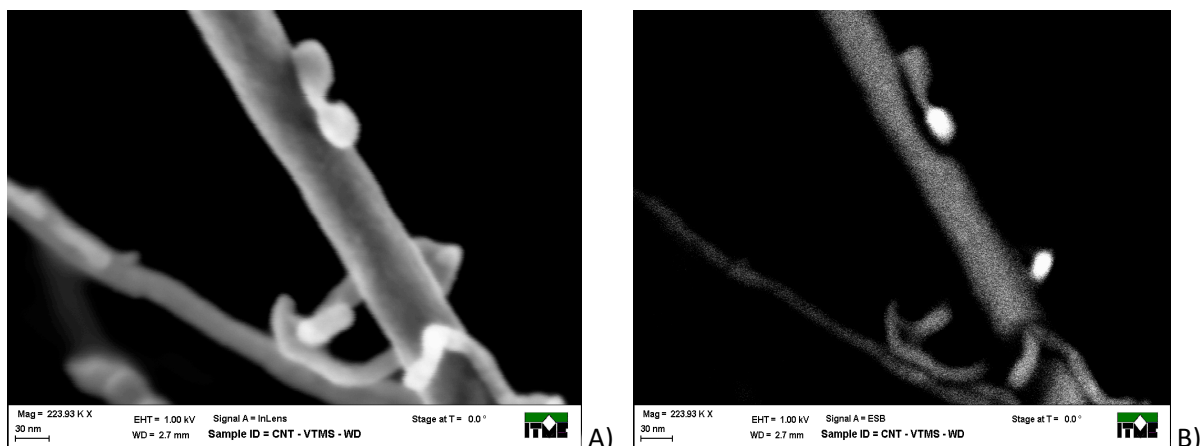


Fig.2 A) SEM image of silane particle etched to the carbon nanotube surface B) SEM - EBS image of silane particle etched to the carbon nanotube surface - bright area indicates on the presence of Si.

Acknowledgment The work has been supported by the Polish National Science Centre within the frame of the grant No DEC-2012/05/B/ST8/02922.

NON- AND WOVEN FLAX FIBER FOR USE IN REINFORCED POLY(BUTYLENE ADIPATE-COTEREPHTHALATE) BIO-COMPOSITES

S. Siengchin^{1,2,4*}, P. Boonyasopon³, R. Srisuk¹, N. Loypetch^{1,4}

¹Department of Materials and Production Engineering, The Sirindhorn International Thai – German Graduate School of Engineering (TGGS), King Mongkut's University of Technology North Bangkok

²Natural Composite Research Group, King Mongkut's University of Technology North Bangkok

³Faculty of Architecture and Design, King Mongkut's University of Technology North Bangkok

⁴Center of Innovation in Design and Engineering for Manufacturing (CoI-DEM), King Mongkut's University of Technology North Bangkok, 1518 Pracharaj 1, Wongsawang Road, Bangsue, Bangkok 10800, Thailand

* to whom correspondence should be addressed (E-mail: suchart.s.pe@tggs-bangkok.org)

Abstract:

Eco-friendly biocomposite materials have been developed from biodegradable polymers as matrices and natural fibers as reinforcement, which have been a good alternative interest in the composite science because of their degradation in soil or regard to environmental condition and do not emit and leave any noxious components on the earth (Teo et al., 2014). Great research efforts are undertaken to produce lightweight, easy reprocessable, especially biocomposites, which may compete with traditional composites in various application fields based on their favored recycling and beneficial performance/cost balance microbiology (Lee et al., 2006). The textile biocomposites made from woven and non-woven flax fibre reinforced poly(butylene adipate-co-terephthalate) (PBAT) were prepared by compression molding using film stacking method (cf-figure 1). The mechanical properties (such as tensile strength and stiffness, flexural strength and modulus, and impact strength) of textile biocomposites were determined in tensile, flexural and impact tests, respectively. The PBAT-based composites were subjected to water absorption. The comparison of the mechanical properties was made between pure PBAT and textile composites. The influence of flax weave styles on the mechanical properties was also evaluated. The results showed that the strength of the textile biocomposites was increased according to weave types of fibers, especially in the stiffness was significantly increased with the higher densification of the fibers. The 4x4-plain woven fibers (4-yard-wrap and 4-yard-weft weave direction) reinforced biocomposite indicated the highest strength and stiffness compared to the other textile biocomposites and pure PBAT. This was considered to be as the result of the character of weave style of 4x4-plain woven fibers. The aminopropyltriethoxysilane affected the mechanical properties and water absorption of the resulting composites laminates due to the surface compatibility between flax fiber and PBAT.

Keywords: biocomposites, PBAT, silane, woven flax fibers, mechanical properties, water uptake.

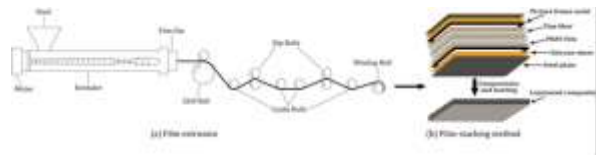


Figure 1: Schematic representation of fabrication procedure of the laminated biocomposite.

Materials:

Poly(butylene adipate-co-terephthalate) (PBAT) pellets were purchased from Ecoflex-FBX7011-BASF. PBAT has a density of 1.25-1.27 g/cm³, the melting temperature of 110-120 °C and transparency of 82% (according to suppliers' information). Woven and non-woven flax fibers used as reinforcement were supplied by Composites Evolution (Chesterfield, UK) and Tilsatec Advanced Materials, Tilsatec Ltd., (Wakefield, UK), respectively. The surface of flax fibers was modified with a 3-Aminopropyltriethoxysilane (APS) coupling agent (Dynasylan® AMEO, Evonik Industries AG, Germany).

Results and discussion:

Morphology

SEM micrographs of the fracture surface of the untreated and treated flax composites are shown in figures 2a-f. SEM micrographs of figures 2(a), (c) and (e) indicates that there were voids between fiber and matrix which was an evidence of poor adhesion. Poor adhesion seems to facilitate debonding of the fiber. This was also confirmed by the mode of fracture in the untreated composites. SEM micrographs of the 3% APS treated flax composite clearly indicated that the treatment facilitated better adhesion

between fiber and matrix than that of untreated one. This was evident that the treatment of flax fiber with APS improved the interfacial adhesion attributing to better strength and stiffness. Note that for selected spots of specimen, an elemental analysis was performed. EDS revealed the major constituents of silane (Si), as indicated in figure 2b. This finding confirms that the APS emerged from the flax fiber.

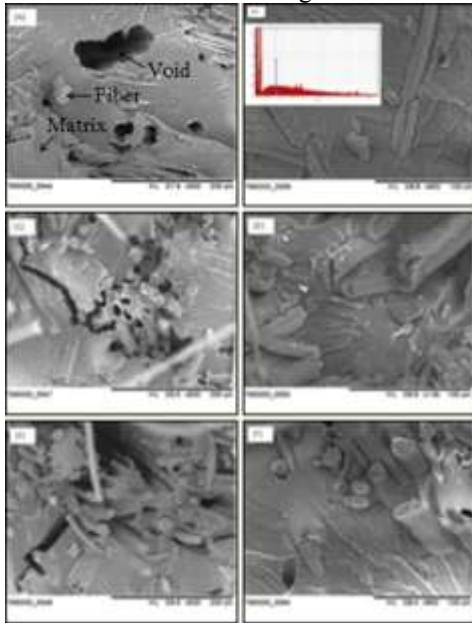


Figure 2: SEM micrographs of the fracture surface of PBAT-flax fiber composites: (A) Untreated and (B) 3% APS treated non-woven flax; (C) Untreated and (D) 3% APS treated 2x2 twill weave flax; (E) Untreated and (F) 3% APS treated 4x4 plain weave flax.

Thermogravimetric analysis

Figure 3 presents the overall thermogravimetric decomposition process for the PBAT and its composites at a heating rate of 10°C/min. It is clearly seen that the thermal decomposition process of the neat PBAT and the 2x2 twill weave flax composites with and without APS treatment had similar characteristics as a result of one-step procedure representing depolymerization. Note that the thermal decomposition of PBAT/APS treated flax composite observed with a slight improvement at high temperature, compared to the treated flax composite. This indicates the effect of APS treated flax on thermal resistance.

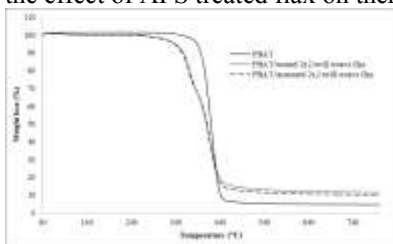


Figure 3: Weight loss versus temperature for the PBAT and its composites.

Dynamic mechanical analysis

Figure 4 depicts the storage modulus (E') and mechanical loss factor ($\tan \delta$) as a function of temperature for the PBAT/2x2 twill weave flax composites with and without APS treatment. One can notice that the storage modulus versus temperature trace of the untreated flax/PBAT composite was always below that of the APS treated flax/PBAT composite. This can be attributed to the improvement of compatibility and interfacial bonding of PBAT/2x2 twill weave flax as discussed earlier.

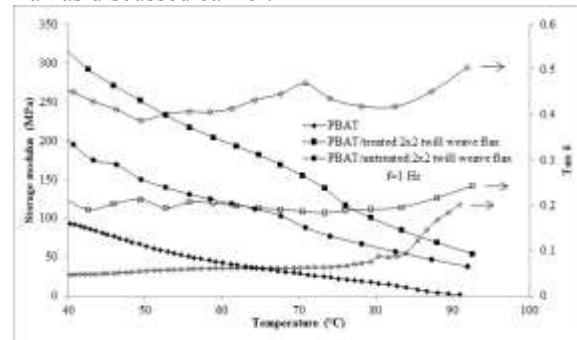


Figure 4: E' , $\tan \delta$ versus T traces for the PBAT and its composites.

Conclusion

The morphology, thermal and mechanical characteristics of composite laminates made from PBAT and woven flax fibers have been investigated. The textile PBAT composites exhibited promising mechanical properties. The incorporation of APS treatment flax enhanced the interfacial bonding, thermal resistance and stiffness of the PBAT based composites.

Acknowledgement

The authors are grateful to Natural Composites Research Group (NCR) for laboratory support. This work was financially supported by the National Research Council of Thailand (NRCT) under the grant agreement KMUTNB-GOV-59-53.

References:

- Teo, P. S., Chow, W. S. (2014) Water vapour permeability of poly (lactic acid)/chitosan binary and ternary blends. *KMUTNB: International Journal of Applied Science and Technology*, 7(1), 23–27.
- Lee, S.H., Wang, S. (2006) Biodegradable polymers/bamboo fiber biocomposite with bio-based coupling agent, *Compos. Part A*, 37, 80-91.

